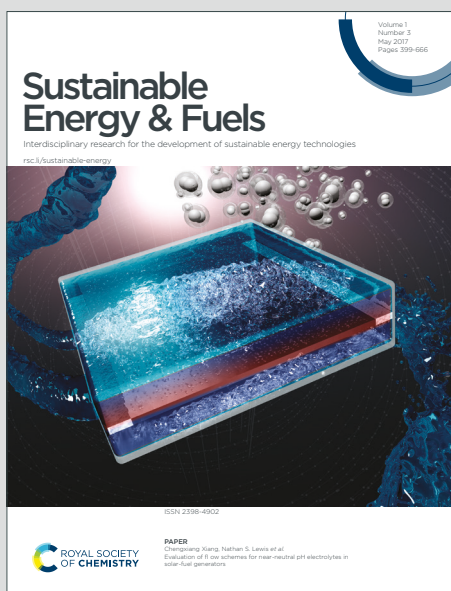


# Sustainable Energy & Fuels

Interdisciplinary research for the development of sustainable energy technologies

Accepted Manuscript

This article can be cited before page numbers have been issued, to do this please use: H. E. M. Hussein, P. Kechagiopoulos and A. Cuesta, *Sustainable Energy Fuels*, 2026, DOI: 10.1039/D5SE01488C.



This is an Accepted Manuscript, which has been through the Royal Society of Chemistry peer review process and has been accepted for publication.

Accepted Manuscripts are published online shortly after acceptance, before technical editing, formatting and proof reading. Using this free service, authors can make their results available to the community, in citable form, before we publish the edited article. We will replace this Accepted Manuscript with the edited and formatted Advance Article as soon as it is available.

You can find more information about Accepted Manuscripts in the [Information for Authors](#).

Please note that technical editing may introduce minor changes to the text and/or graphics, which may alter content. The journal's standard [Terms & Conditions](#) and the [Ethical guidelines](#) still apply. In no event shall the Royal Society of Chemistry be held responsible for any errors or omissions in this Accepted Manuscript or any consequences arising from the use of any information it contains.

1 **Electrochemical conversion of CO<sub>2</sub> plasmas**2 **Haytham E. M. Hussein,<sup>a,d</sup> Panagiotis N. Kechagiopoulos,<sup>b,\*</sup> Angel Cuesta<sup>a,c,\*</sup>**3 <sup>a</sup>Advanced Centre for Energy and Sustainability (ACES), School of Natural and  
4 Computing Sciences, University of Aberdeen, AB24 3UE Aberdeen, Scotland, UK,5 <sup>b</sup>Chemical Processes & Materials Group, School of Engineering, University of  
6 Aberdeen, Aberdeen AB24 3UE, UK7 <sup>c</sup>Instituto de Química Física Blas Cabrera, CSIC, C. Serrano 119, E-28006 Madrid,  
8 Spain9 <sup>d</sup>GSK Carbon Neutral Laboratories for Sustainable Chemistry, Jubilee Campus,  
10 Wollaton Road, University of Nottingham, Nottingham, NG8 1BB, UK11  
12 E-mail: [p.kechagiopoulos@abdn.ac.uk](mailto:p.kechagiopoulos@abdn.ac.uk); [angel.cuestaciscar@abdn.ac.uk](mailto:angel.cuestaciscar@abdn.ac.uk);  
13 [acuesta@iqf.csic.es](mailto:acuesta@iqf.csic.es)14 **Abstract**15 The integration of non-thermal CO<sub>2</sub> plasma (NTP) with a custom-designed electrolyte-  
16 gap electrolyser and CuO catalysts represents an innovative strategy to enhance the  
17 electrochemical conversion of CO<sub>2</sub> into C1–C3 products. Systematic galvanostatic  
18 experiments conducted at current densities ranging from 100 to 225 mA cm<sup>-2</sup>  
19 demonstrated that plasma-on operation significantly reduces cell voltages (by up to  
20 ~1.3 V) and that product selectivity transitions from C1 species (CO and methane) to  
21 C2+ products, including ethylene, ethanol, acetate, propylene, and propanol. While  
22 CO and H<sub>2</sub> predominate under plasma-off conditions, with limited formation of C2  
23 products, the hybrid plasma–electrochemical system increases the Faradaic efficiency  
24 (FE) for ethylene up to 39.5% and ethanol up to 18.1%. These enhancements are  
25 attributed to plasma-generated reactive species (radicals and excited-state molecules)  
26 that lower kinetic barriers for C–C coupling and modify the interfacial pH, thereby  
27 reducing parasitic carbonate/bicarbonate losses. The plasma-on state resulted in a  
28 statistically significant increase in liquid product carbon efficiency (from an average of  
29 ~0.41% during plasma-off experiments to ~0.91% during plasma-on experiments).  
30 Although the system currently exhibits lower overall energy efficiency owing to the

1 power demands of the plasma discharge, this work establishes a robust framework for  
2 flexible product tuning and sustainable carbon utilisation via plasma-activated feeds.

3

#### 4 **Keywords**

5 CO<sub>2</sub> electrochemical conversion, Plasma, Electrocatalysis, CO<sub>2</sub> reduction reactions,  
6 Energy Conversion, Fuel Production

#### 7 **Introduction**

8 The electrochemical conversion of CO<sub>2</sub> into value-added chemicals and fuels —  
9 specifically C<sub>2</sub> and C<sub>3</sub> products — and their scalability can aid efforts to decelerate  
10 climate change and produce chemicals from sources alternative to crude oil and  
11 gases.<sup>1</sup> Many studies have explored the electrocatalytic conversion of CO<sub>2</sub>,  
12 emphasising the importance of transition metal surfaces such as Cu in converting CO<sub>2</sub>  
13 into valuable chemicals such as methane, ethylene, and ethanol.<sup>2-5</sup>

14 Lab-scale electrochemical CO<sub>2</sub> conversion typically uses flow cells with either an  
15 electrolyte-gap-membrane electrode assembly (MEA) or a zero-gap MEA,<sup>6-9</sup> because  
16 gas diffusion electrodes (GDEs) allow overcoming the low solubility of CO<sub>2</sub> in the most  
17 commonly used solvent, water. Research focuses on developing and optimising the  
18 catalyst,<sup>10-12</sup> the electrolyte composition,<sup>13-15</sup> the pH,<sup>16-20</sup> the operating temperature,<sup>21</sup>  
19 and the polymer-electrolyte membrane in the MEA.<sup>22</sup>

20 For instance, Gonçalves et al.<sup>23</sup> demonstrated the selective production of C<sub>2</sub>  
21 hydrocarbons, particularly ethylene, using copper electrodes modified via  
22 electroplating. Gao et al.<sup>24</sup> investigated the effect of designing and modifying  
23 electrocatalyst structures, the influence of electrolytes on selectivity and conversion  
24 rate, and the potential applications of electrolyzers for large-scale CO production.  
25 Other studies have explored the possible integration of CO<sub>2</sub> conversion processes with  
26 renewable energy sources, such as the work by Kauffman et al.<sup>25</sup> to increase reaction  
27 rates and product selectivity.

28 Cu and Cu-based materials are the most common catalysts capable of  
29 electrocatalytically reducing CO<sub>2</sub> beyond C<sub>1</sub> products, such as CO/HCOOH, with  
30 significant Faradaic efficiency (*FE*).<sup>26, 27</sup> This functional property stems from Cu's



1 ability to activate C–C coupling through CO adsorption.<sup>28</sup> Nonetheless,  
2 electrochemical CO<sub>2</sub> conversion using Cu often requires high overpotentials to  
3 achieve a reasonable reaction rate and selectivity towards C<sub>2</sub><sup>+</sup> products, limiting the  
4 practical applications of Cu catalysts.<sup>29</sup> Furthermore, applying high current densities  
5 or high overpotentials leads to the detachment of the catalysts or rapid deactivation,  
6 in addition to competition with the hydrogen evolution reaction (HER).<sup>29-31</sup>

7 Several mechanisms have been proposed to explain the production of C<sub>2</sub><sup>+</sup> products  
8 at the Cu surface. Surface oxygen species and electrophilic Cu<sup>δ+</sup> species with low  
9 coordination in oxide-derived materials are assumed to play a critical role in the activity  
10 and selectivity for C<sub>2</sub><sup>+</sup> production.<sup>32</sup> Research work has suggested that Cu<sup>+</sup>/Cu<sup>0</sup>  
11 surface species promote CO<sub>2</sub> conversion to C<sub>2</sub><sup>+</sup> products due to an enhanced ability  
12 for CO<sub>2</sub> activation and C–C coupling.<sup>24, 33 24, 33</sup> On the other hand, recent studies have  
13 focused on controlling the local surface electronic structure by combining surface Cu  
14 with other metal atoms in atomic proximity,<sup>34, 35</sup> to promote C–C coupling on  
15 asymmetric atom pairs, thus accelerating C<sub>2</sub><sup>+</sup> production by CO dimerisation.<sup>34, 35</sup>  
16 However, bimetallic systems such as CuAg, CuPd, and CuAu promote forming C<sub>1</sub>  
17 products over C<sub>2</sub> products, and show poor selectivity.<sup>34, 35</sup> Furthermore, production of  
18 C<sub>3</sub> terminal oxygenates (*e.g.*, propanol) and hydrocarbons (*e.g.*, propylene) has been  
19 reported in only a few studies, with reaction mechanisms that are controlled by the  
20 presence of specific intermediates such as \*OCH<sub>2</sub>CH<sub>3</sub> or the coupling between  
21 adsorbed/molecular carbon dioxide or carboxyl with the \*C<sub>2</sub> intermediates that are  
22 involved in the ethylene pathway.<sup>13, 36</sup>

23 One of the key advantages of electrochemical CO<sub>2</sub> conversion is its flexibility in  
24 adjusting the product distribution and its potential for modular design. This adaptability  
25 allows us to tailor reactor designs for specific applications, making it an attractive  
26 option for carbon-intensive manufacturing industries seeking to use renewable energy  
27 for CO<sub>2</sub> conversion. Hence, to improve reactor engineering for CO<sub>2</sub> electrochemical  
28 reduction, research has focused on managing the reactants and flow cell  
29 architectures. However, CO<sub>2</sub> is a thermodynamically stable molecule, making its  
30 conversion into chemicals or fuels an energy-intensive process. Recently, a  
31 combination of electrochemical reactions with a non-thermal plasma (NTP) has been  
32 used to convert N<sub>2</sub> into ammonia.<sup>37</sup> Similarly, the hybridisation of a dielectric barrier  
33 discharge and a solid oxide electrolyser cell has been used to convert CO<sub>2</sub>.<sup>38</sup> NTPs



1 generate energetic electrons that activate small molecules, such as CO<sub>2</sub> and N<sub>2</sub>, under  
2 ambient conditions, and subsequent electrocatalysis enables the selective formation  
3 of products under mild conditions. Combining both approaches may enhance the  
4 conversion efficiency, selectivity, and energy utilisation. For instance, in the work by  
5 Kumari et al.,<sup>37</sup> the plasma-assisted electrochemical system produced 47% more  
6 ammonia than the sum of the plasma-only and electrochemical-only conditions. In this  
7 work, we investigated the impact of the nature of the CO<sub>2</sub> feed on the conversion  
8 activity and selectivity for producing C<sub>2</sub><sup>+</sup> by engineering a lab-scale reactor that can  
9 be fed with either CO<sub>2</sub> or a CO<sub>2</sub> NTP at the cathode. Our research revealed that  
10 activated CO<sub>2</sub> species, including vibrationally excited CO<sub>2</sub> molecules and neutral and  
11 ionic radicals, play a role in enhancing the electrochemical conversion of CO<sub>2</sub> into C<sub>2</sub><sup>+</sup>  
12 gas and liquid products. By addressing these key areas, we aim to develop reactor  
13 architectures and system engineering strategies that will enable further advancements  
14 in CO<sub>2</sub> conversion technology and inspire potential industrial applications.

## 15 Experimental

16 **Chemicals.** Cesium hydrogen carbonate, 99.99%, (CsHCO<sub>3</sub>, Thermo Scientific  
17 Chemicals), cesium methanesulfonate, 98%, (Cs(SO<sub>3</sub>CH<sub>3</sub>), Thermo Scientific  
18 Chemicals), and cesium sulfate, 99+% pure, (Cs<sub>2</sub>SO<sub>4</sub>, Thermo Scientific Chemicals)  
19 were used to prepare the electrolyte. The electrolyte composition was 0.5 M CsHCO<sub>3</sub>  
20 + 0.25 M Cs(SO<sub>3</sub>CH<sub>3</sub>) + 0.25 M Cs<sub>2</sub>SO<sub>4</sub> in water. The choice of Cs<sup>+</sup> is consistent with  
21 cation–size–driven field effects that stabilise dipolar intermediates on Cu and can  
22 promote multi-carbon products.<sup>1, 39-41</sup> In addition, this mixture of salts minimises the  
23 formation of carbonate and bicarbonate during the electrochemical reduction of CO<sub>2</sub>.<sup>14,</sup>  
24 <sup>42</sup> Note that while alkali metal cations are traditionally viewed as chemically inert, their  
25 hydration shells undergo significant polarisation within the high-strength electric field  
26 of the electrical double layer (EDL).<sup>42, 43</sup> Although the bulk pK<sub>a</sub> of hydrated Cs<sup>+</sup> is  
27 approximately 14.7, the intense interfacial field effectively lowers this value at the  
28 electrode surface.<sup>44</sup> This allows larger cations to mitigate the accumulation of OH<sup>-</sup>  
29 generated during reduction.<sup>45-47</sup> By maintaining the interfacial pH within a range that  
30 favours molecular CO<sub>2</sub> stability (typically <9-10), this buffering effect prevents the  
31 competitive shift toward non-reducible carbonate species<sup>48</sup>: CO<sub>2</sub> + 2OH<sup>-</sup> → CO<sub>3</sub><sup>2-</sup> + H<sub>2</sub>O.



1 The choice of methanesulfonate ( $\text{CH}_3\text{SO}_3^-$ ) as a spectator electrolyte is supported by  
2 its high cathodic stability compared to the targeted  $\text{CO}_2\text{RR}$  and the competing  
3 hydrogen evolution reaction (HER).<sup>46, 49</sup> The reductive cleavage of the  
4 methanesulfonate C-S bond occurs at significantly more negative potentials  
5 (approximately -1.5 V vs. RHE), ensuring that the anion remains intact. Unlike halides,  
6 the "hard" nature of the sulfonate group results in negligible specific adsorption,  
7 preserving the catalyst's active sites for  $\text{CO}_2$  intermediates ( $^*\text{COOH}$ ,  $^*\text{CO}$ ).<sup>49</sup>

8 Cupric oxide (CuO, 99.9%) and iridium (IV) oxide ( $\text{IrO}_2$ , 99.9%) nanoparticle catalysts  
9 were purchased from Sigma Aldrich. All aqueous electrolytes used in this study were  
10 prepared using 18 M $\Omega$  cm water (Thermo, smart2pure). All chemicals were used as  
11 received without further purification.

12 Preparation of the electrodes and membranes. The cathodes were fabricated by  
13 spraying the catalyst ink onto the gas diffusion layer (GDL; Fuelcellstore,  
14 Sigracet 39 BB, a non-woven carbon paper microporous layer (MPL) that had been  
15 treated with PTFE to 5 wt%). The catalyst ink was prepared by suspending 30 mg of  
16 commercial CuO nanoparticles in a mixture of 500  $\mu\text{L}$  of isopropanol and 200  $\mu\text{L}$  of  
17 water. The catalyst ink was then stirred overnight to ensure uniform mixing and  
18 sprayed onto Sigracet 39 BB at room temperature using a Neo for Iwata TRN1 gravity  
19 feed airbrush. A similar procedure was used to prepare the anode; however, CT  
20 carbon cloth was used with MPL (Fuelcellstore) as the GDL instead of Sigracet 39 BB,  
21 and  $\text{IrO}_2$  was used as the catalyst. The anode catalyst ink was also modified by adding  
22 1  $\mu\text{L}$  of a binder solution of 5% PTFE dissolved in isopropanol. A piperION<sup>®</sup> Anion  
23 Exchange Membrane (AEM; Fuelcellstore), 20  $\mu\text{m}$  thick, self-supporting, was used as  
24 the membrane separating the anode and cathode. The AEM was immersed in  
25 1 M  $\text{CsHCO}_3$  for 48 h and then washed with deionised water several times before use  
26 in the electrolyser. Scanning electron microscopy (SEM) images and energy-  
27 dispersive X-ray spectroscopy (XEDS) data of the anode and cathode are shown in  
28 S1, Fig. S1.

29 Electrolysers. The electrolyte gap electrolyser was custom-made using a flow cell  
30 setup, as illustrated in Figs. 1 and S2. A 3 mm thick catholyte flow field compartment  
31 (3D printed, Tough 2000 Resin, Formlabs) was placed between the cathode gas  
32 diffusion electrode (GDE) and the AEM (Figs. 1 and S2). A 3 mm-thick gas flow field



1 was introduced between a rigid 3D-printed PEEK plate (identified as a gas chamber  
2 in Figs. 1 and S2, 8 mm thick, Rigid 10 K Resin, Formlabs) and the cathode GDE. The  
3 gas flow field and chamber fed the reactant, either CO<sub>2</sub> gas or CO<sub>2</sub> NTP, to the  
4 cathode. The anolyte and catholyte comprised the same electrolyte solution,  
5 consisting of 0.5 M CsHCO<sub>3</sub>, 0.25 M Cs(SO<sub>3</sub>CH<sub>3</sub>), and 0.25 M Cs<sub>2</sub>SO<sub>4</sub> in water, and  
6 were circulated to the anode and cathode, respectively. The cathode GDE, which is  
7 sandwiched between two gaskets, separates the catholyte flow field from the cathode  
8 CO<sub>2</sub> gas/CO<sub>2</sub> NTP chamber. The CuO catalyst layer faces the catholyte compartment,  
9 whereas the CO<sub>2</sub> gas/CO<sub>2</sub> NTP flows on the opposite side of the PTFE-treated  
10 MPL/GDL.

11 Carbonate/bicarbonate quantification was performed *ex situ* using electrolyte samples  
12 collected from the outlet streams during galvanostatic operation. Samples were  
13 collected over defined time windows, sealed to minimise CO<sub>2</sub> exchange with air, and  
14 analysed by two-step acid titration (first endpoint ~pH 8.3; second endpoint ~pH 4.5).

15

16



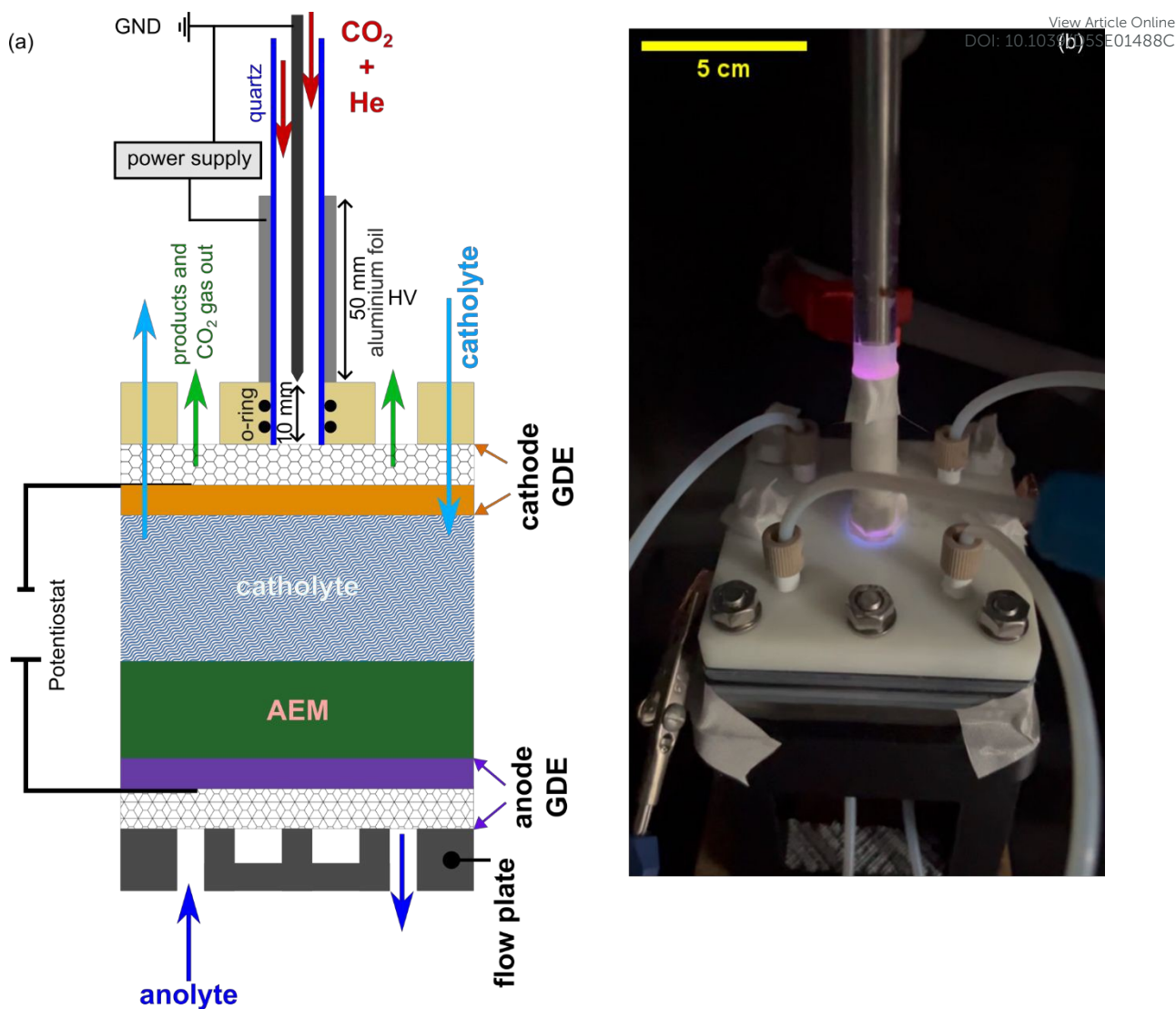


**Figure 1.** (a) A schematic representation of the electrolyte-gap electrolyser showing the interface between the CO<sub>2</sub> NTP DBD and the cathode GDE. (i) quartz tube (7 mm ID / 9 mm OD) with coaxial DBD electrodes (internal grounded stainless-steel rod; external HV foil), (ii) 50 mm long HV foil, axially positioned 10–60 mm upstream of tube exit, (iii) the exit plane of the glass tube is levelled with the bottom side of the housing plate, the plasma input was secured and sealed gas-tight by compressing two Viton O-rings and (iv) the distance from the grounded rod tip to the cathode surface is 10 mm. (b) Photograph of the experimental set-up showing the plasma ignition during the CO<sub>2</sub> conversion experiments.

2

3 The geometric area of the cathode, which was used to calculate the current density,  
 4 was 1 cm<sup>2</sup>. CO<sub>2</sub> (99.999%, BOC) was fed to the cathode, and a 1 M solution of mixed  
 5 Cs (the electrolyte) was flowed to both the cathode and anode. The gas products were  
 6 analysed using a gas chromatograph (GC, Thermo Scientific, Trace1300) equipped



1 with a thermal conductivity detector (TCD) and a ShinCarbon ST micropacked column  
2 (100/120, 2 m, 1 mm ID). Ultra-high-purity He (99.9999%, BOC) or high-purity N<sub>2</sub>  
3 (99.99%) was used as the carrier gas. The TCD detected H<sub>2</sub> using N<sub>2</sub> as the carrier  
4 and carbon-containing products (unreacted CO<sub>2</sub>, CO, CH<sub>4</sub>, C<sub>2</sub>H<sub>4</sub>, C<sub>2</sub>H<sub>6</sub>, and C<sub>3</sub>H<sub>6</sub>)  
5 using He as the carrier. A trap jar filled with cold water was installed after the cell  
6 output channel to examine the liquid products. The anolyte, catholyte, and water in the  
7 water trap were syringed out and analysed using ultra-high-performance liquid  
8 chromatography (UHPLC, UltiMate3000, Thermo Scientific) equipped with a refractive  
9 index, variable wavelength detector, and HyperREZ™ XP carbohydrate H+ LC  
10 Column. Electrochemical control was achieved using a Parstat MC potentiostat  
11 (Princeton Applied Research, Ametek SI)

12 CO<sub>2</sub> plasma experiments. A dielectric barrier discharge (DBD) non-thermal plasma  
13 (NTP) was generated using a coaxial electrode configuration inside a quartz tube  
14 (inner diameter: 7 mm; outer diameter: 9 mm). A 6.35 mm diameter stainless-steel rod  
15 placed along the tube axis served as the grounded electrode, while an aluminium foil  
16 wrapped around the outer wall of the quartz tube served as the high-voltage (HV)  
17 electrode. The HV foil length was 50 mm, and it was positioned axially 10–60 mm  
18 upstream of the tube exit plane (*i.e.* the downstream foil edge was 10 mm upstream  
19 of the tube exit). The DBD reactor was interfaced with the electrochemical CO<sub>2</sub> flow  
20 cell by inserting the quartz tube through a 3D-printed plate on the back of the cathode  
21 side of the electrolyser as shown in Fig. 1 and S2, Fig. S2. The desired gases (CO<sub>2</sub>,  
22 and He) flowed through the quartz tube at flow rates determined by Mass Flow  
23 Controllers (MFC) from Sensirion (SFC5500) and MKS (1179A). The plasma was  
24 driven by a high-voltage AC power supply (PVM500-2500) operating at a sinusoidal  
25 waveform of ~40 kHz. The voltage and charge were sampled using an HV probe (Cal  
26 Test CT4028) and a passive probe (Teledyne LeCroy PP020) that measured the  
27 voltage across a 9.671 nF ceramic capacitor connected to the ground line,  
28 respectively. Both probes were connected to a 100 MHz digital oscilloscope (B&K  
29 Precision 2194). All reported plasma measurements were performed at an applied  
30 power of 10 ± 0.5 W, estimated from the voltage and charge data by integrating the  
31 Q-V Lissajous plot (see S3, Figs. S3 and S4). The DBD reactor was interfaced with  
32 the electrochemical CO<sub>2</sub> flow cell by inserting the quartz tube through a 3D-printed  
33 plate on the back of the cathode side of the electrolyser, with a hole that fits the 9 mm



1 outer diameter of the quartz tube. The plasma input into the cathode was secured and  
2 sealed gas-tight using compression of two Viton O-rings. The distance from the  
3 internal DBD electrode's tip to the cathode's surface was 10 mm. To ensure safe  
4 operation, the external high-voltage (HV) foil electrode and its electrical connection  
5 were fully insulated using a silicone sleeve, and 3M Scotch Cloth Tape with a glass  
6 finish was applied to cover the aluminium foil. The integrated plasma–electrolyser  
7 assembly was enclosed within a non-conductive polycarbonate housing. The internal  
8 surfaces of the housing were coated with an electromagnetic interference (EMI)  
9 shielding spray and grounded to mitigate external electromagnetic interference. The  
10 HV power supply was equipped with a hardware enable/disable switch, and a single-  
11 point grounding scheme was implemented to prevent unintended returns. The  
12 maximum applied voltage is 12 kV peak-to-peak (pk-pk), although the maximum  
13 possible voltage is 30 kV pk-pk. The flow rates were regulated by mass flow  
14 controllers, with CO<sub>2</sub> flow at 30 NmL min<sup>-1</sup> and He flow at 5 NmL min<sup>-1</sup>, resulting in a  
15 total flow of 35 NmL min<sup>-1</sup>. Given the inner diameter of the quartz tube, which  
16 measures 7 mm, this configuration corresponds to a nominal average linear velocity  
17 of approximately 1.52 cm s<sup>-1</sup> within the tube under standard conditions (ideal gas).  
18 Considering the coaxial configuration, with a 7 mm inner diameter tube and a 6.35 mm  
19 rod, the annular cross-sectional area is calculated to be 6.8×10<sup>-6</sup> m<sup>2</sup>. This  
20 configuration yields a nominal annular gas velocity of approximately 8.6 cm s<sup>-1</sup>.

21 Experiment for preheating the CO<sub>2</sub> feed. In experiments focused on thermal control,  
22 the CO<sub>2</sub> feed was elevated to a temperature of 150 °C using an Omega heating tape  
23 (1.245 kW, 240 VAC, 1" × 8") installed upstream of the electrolyser. The temperature  
24 was controlled by a PID controller, and a K-type thermocouple, positioned just before  
25 the cathode gas inlet, was used to monitor the gas temperature. To prevent heat loss  
26 before the gas entered the cell, the heated gas line was insulated. This setup was  
27 used to evaluate whether the selectivity and voltage fluctuations observed during  
28 plasma-on operation were solely due to the increased temperature of the reactants.

29 Physical and chemical characterisation. Scanning electron microscopy (SEM) and  
30 energy-dispersive X-ray spectroscopy (XEDS) were performed using a Zeiss  
31 microscope at an operating voltage of 10 kV to image the morphology of the electrodes  
32 and at 15 kV to analyse the chemical composition of the catalysts before and after the  
33 experiments. Optical emission spectroscopy (OES) was used to identify the active



1 species in the CO<sub>2</sub> plasma, as shown in Figs. S3, S5, and Table S1. OES was  
2 conducted using an Avantes 5-Channel ULS4096CL-EVO AvaSpec rackmount  
3 spectrometer, with each channel specified independently to achieve a resolution of 0.1  
4 nm across a broad wavelength range of 190 to 900 nm (grating of 1800 lines/mm for  
5 190–350 nm, 349–500 nm, 499–643 nm, 642–733 nm, and 1200 lines/mm for 732–  
6 905 nm). Emission was collected under conditions equivalent to the experimental  
7 conditions using a five-furcated cable comprising five ×200 μm optical fibres,  
8 positioned inside the reactor tube downstream of the discharge. Spectra were  
9 acquired with an integration time of 30 s and averaged over three scans with dark-  
10 background subtraction applied. Wavelength calibration was performed using a  
11 calibration source (neon lamp).

## 12 Results and Discussion

13 An AC power source was employed to generate CO<sub>2</sub> NTP. The gas feed through the  
14 DBD tube comprised CO<sub>2</sub> at a flow rate of 30 NmL min<sup>-1</sup> combined with He at 5 NmL  
15 min<sup>-1</sup>. In the plasma-off experiments, the cathode feed composition remained  
16 identical; however, the AC power supply was deactivated. In this context, "plasma-off"  
17 denotes conventional electrochemical CO<sub>2</sub> reduction (eCO<sub>2</sub>) using molecular gas,  
18 whereas "plasma-on" refers to the electrolysis of the CO<sub>2</sub> NTP effluent. Given that the  
19 cathode is positioned downstream of the DBD discharge region, with the grounded rod  
20 tip situated 10 mm from the cathode (*that is*, the GDE plane), the catalyst is primarily  
21 exposed to post-discharge (afterglow) species emanating from the quartz tube rather  
22 than the high-field microdischarge region.<sup>37</sup> Consequently, the flux and lifetime of  
23 activated neutrals, such as vibrationally excited CO<sub>2</sub>/CO and radical species, during  
24 their transport from the discharge to the GDE, are critical in determining plasma-  
25 electrode coupling.<sup>50-55</sup> Furthermore, the current design allows for the flow to expand  
26 across the entire area of the GDE, thereby preventing localised concentration  
27 gradients. Initially, upon NTP ignition and without operating the electrochemical cell to  
28 facilitate CO<sub>2</sub> conversion into fuel, we observed the typical products of the CO<sub>2</sub> NTP,<sup>50,</sup>  
29 <sup>56, 57</sup> specifically CO<sub>2</sub>, CO, and oxygen, S3, Fig. S6. We then recorded the cell voltage  
30 under zero net current conditions to study the electrical coupling control. As depicted  
31 in Fig. S7, electrical coupling control was performed before galvanostatic electrolysis,  
32 with the plasma being alternately activated and deactivated (10 min. on and 10 min.  
33 off) while the cell voltage vs. time (potentiostat log) was recorded. The trace was



1 scrutinised for any synchronous modulation associated with the ~40 kHz high-voltage  
2 (HV) waveform.

3 **Electrocatalytic performance and product selectivity transitions.** The  
4 electrocatalytic activity was initially evaluated by collecting linear sweep  
5 voltammograms (LSV) at 50 mV s<sup>-1</sup> under plasma-on and off conditions, as shown in  
6 Fig. 2(a). The LSV (red curve) recorded under plasma-off conditions shows no  
7 cathodic peak, and the cathodic current begins to increase at a voltage more negative  
8 than -0.7 V vs. RHE due to CO<sub>2</sub> electrochemical reduction and HER, with the current  
9 rapidly rising above -0.8 V vs. RHE. In contrast, during plasma-on (CO<sub>2</sub> NTP DBD)  
10 experiments, the LSV (black curve) displayed a cathodic peak ( $E_{\text{reduction}} = -0.75$  V vs.  
11 RHE), and the cathodic current commenced to increase negatively from -  
12 0.15 V vs. RHE due to electrochemical conversion of species in the CO<sub>2</sub> NTP, in  
13 addition to HER. Simultaneously, we monitored the production rates of various  
14 gaseous and liquid products to assess the synergistic integration of CO<sub>2</sub> NTP with  
15 electrochemical CO<sub>2</sub> reduction, as depicted in Fig. 2 (b). In the absence of CO<sub>2</sub> NTP,  
16 *that is*, with the plasma off (Fig. 2 (bi)), the system exhibited high selectivity for C1 gas  
17 products. Carbon monoxide is the predominant product, with its production rate  
18 reaching approximately 0.5 μmol s<sup>-1</sup> cm<sup>-2</sup> at -1.1 V. Hydrogen is the primary byproduct,  
19 with its rate increasing as the overpotential rises.

20 By changing the source and introducing CO<sub>2</sub> NTP DBD (*i.e.*, plasma activation or  
21 plasma on), we observed a shift in the reaction landscape/pathway. Although the CO  
22 production rate remained stable at approximately 0.13 μmol s<sup>-1</sup> cm<sup>-2</sup>, there was a  
23 notable increase in the C2 and C3 product yields. Ethylene emerged as the major  
24 product, with a rate of 0.09 μmol s<sup>-1</sup> cm<sup>-2</sup>. Additionally, a diverse array of liquid  
25 oxygenates (acetate, ethanol, and propanol) and gaseous hydrocarbons (ethane and  
26 propylene) appeared, which were either absent or minimal under the plasma-off  
27 condition.

28

29



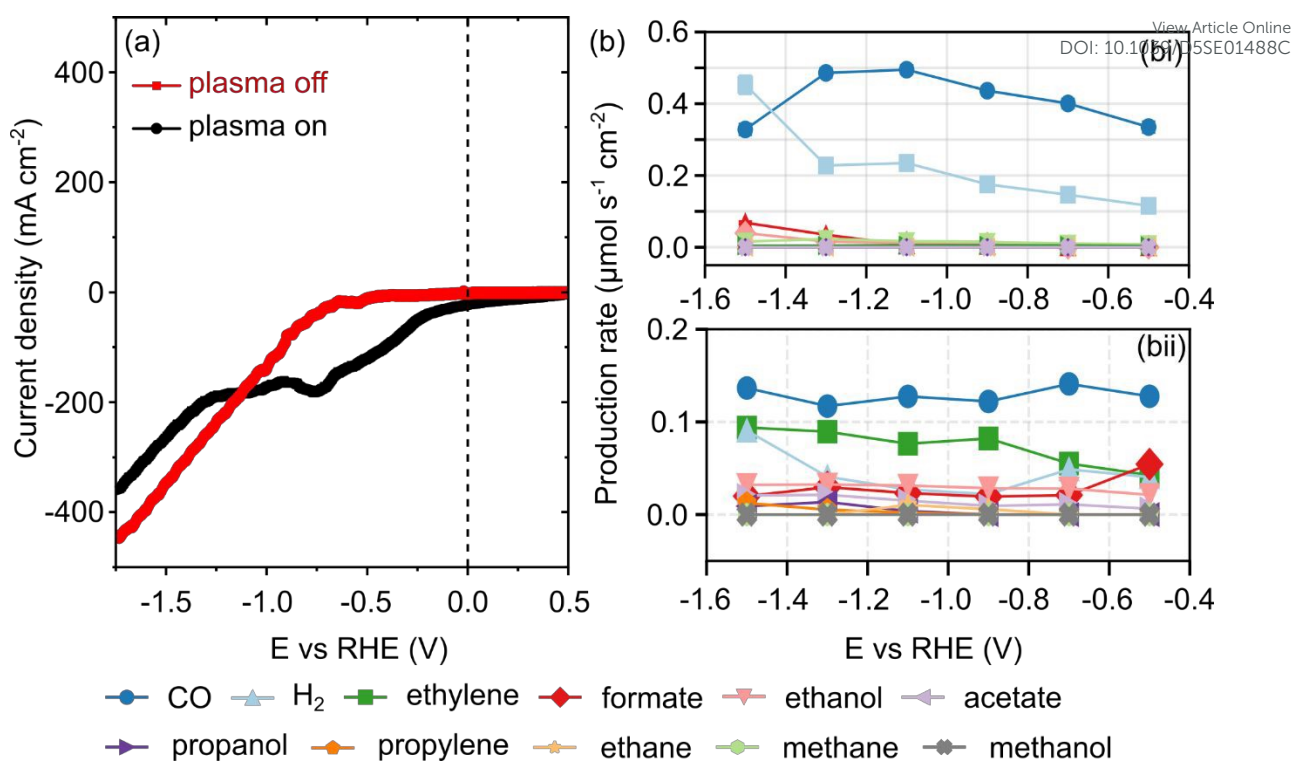


**Figure 2:** Electrocatalytic Performance and Product Selectivity Transitions (a) LSV of CO<sub>2</sub> electrochemical conversion under two conditions: plasma-off (red line) and plasma-on (black line). (b) Production rate of gas and liquid products vs. potential for (bi) electrochemical conversion with plasma-off and (bii) electrochemical conversion with plasma-on.

**Voltage Characteristics and Reaction Kinetics.** To evaluate the performance of CuO under conditions pertinent to industrial applications, we conducted a series of galvanostatic CO<sub>2</sub> reduction reaction (CO<sub>2</sub>RR) experiments across a current density range of 100 to 225 mA cm<sup>-2</sup>, S4, Figs. 8-13 and Table S2 (note Fig. S13 shows an image of the electrode after the electrolysis process). While fundamental laboratory studies frequently employ low current densities (< 10 mA cm<sup>-2</sup>) in H-cell configurations, achieving partial current densities exceeding 200 mA cm<sup>-2</sup> is crucial for the techno-economic feasibility of CO<sub>2</sub> electrolyzers.<sup>58</sup> By utilising a flow-cell architecture equipped with a GDE, we aimed to assess the influence of breaking the strong CO<sub>2</sub> bond by NTP. Galvanostatic control was specifically selected to maintain a constant production rate and to systematically investigate the evolution of the cell potential, which is sensitive to local pH fluctuations and the mechanical integrity of the triple-phase boundary at elevated reaction rates. Moreover, incremental step-wise testing from 100 to 225 mA cm<sup>-2</sup> facilitated a precise mapping of the FE changes, providing



1 critical insights into the onset of competitive HER and the durability of the GDE against  
2 flooding and carbonate precipitation.

3 We investigated the effect of switching between plasma-off and plasma-on conditions,  
4 in which CO<sub>2</sub> gas was constantly fed into the electrolyte gap electrolyser, and the  
5 plasma power was turned on and off in real-time (Fig. 3). By operating the cell at a  
6 fixed current density of 175 mA cm<sup>-2</sup>, the cell exhibited a high operational voltage of  
7 ~4.5 V during the plasma-off phase, and upon switching to the plasma-on mode, the  
8 cell voltage decreased significantly to ~3.5 V (Fig. 3 (a)). The minor voltage drift  
9 observed during the initial plasma-on and subsequent plasma-off intervals is attributed  
10 to transient discharge stabilisation and the associated equilibration of gas transport  
11 and wetting; later segments approach a quasi-steady operational state. The transition  
12 to the plasma-on state significantly impacted the ethylene/carbon monoxide ratio and  
13 promoted the formation of liquid oxygenates (ethanol and acetate), as discussed  
14 below.

15 Under these conditions, as shown in Fig. 3(b), the FE was dominated by CO (FE,  
16 56.3%) and H<sub>2</sub> as a byproduct (FE, 22.2%), with minor contributions from CH<sub>4</sub>, C<sub>2</sub>H<sub>4</sub>,  
17 C<sub>2</sub>H<sub>5</sub>OH, and HCOO<sup>-</sup> (FEs of 5.1%, 3.2%, 8.7%, and 1%, respectively; see S5 and  
18 Equations S5, S1–S5 for FE calculations). Upon switching to the plasma-on mode, a  
19 distinct shift in the product distribution (Fig. 3(b)) was observed. Notably, methane  
20 production was suppressed below the detectable limit, while ethylene and acetate  
21 emerged with FEs of 4.8% and 3.2%, respectively. The activation of the plasma also  
22 markedly enhanced the selectivity toward C<sub>2</sub> species; the FEs of ethane and ethanol  
23 increased to 40.5% and 20.1%, respectively, representing a substantial shift from CO-  
24 dominant to multicarbon-product-dominant electrocatalysis. Furthermore, the  
25 reduction in H<sub>2</sub> FE to 6.2% underscores the efficacy of the CO<sub>2</sub> NTP–electrochemical  
26 hybrid system in suppressing competitive HER and redirecting the electron flux toward  
27 high-value carbon products.



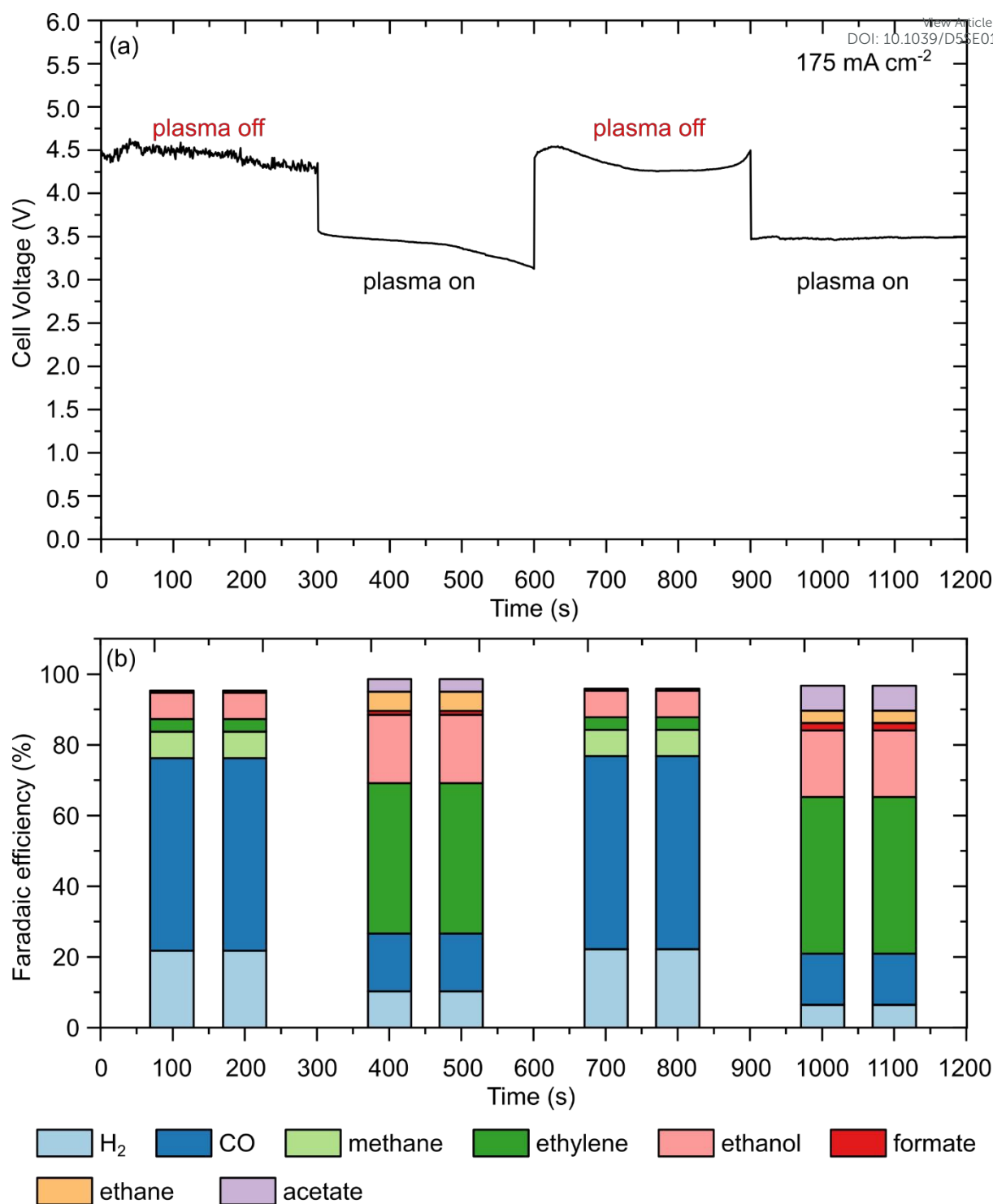


**Figure 3:** Dynamic response of the electrolyte-gap electrolyser to plasma activation. (a) Chronopotentiogram profile at  $175 \text{ mA cm}^{-2}$  of  $\text{CO}_2$  electrolysis using  $\text{CO}_2$  gas and  $\text{CO}_2$  NTP as reactant source, highlighting the voltage reduction ( $\sim 1.0 \text{ V}$ ) upon switching from plasma-off to plasma-on conditions. Galvanostatic experiments were conducted in  $0.5 \text{ M CsHCO}_3 + 0.25 \text{ M Cs(SO}_3\text{CH}_3) + 0.25 \text{ M Cs}_2\text{SO}_4$  aqueous electrolyte. (b) Corresponding FE distribution of products obtained from  $\text{CO}_2$  conversion reaction on CuO catalyst in the flow  $\text{CO}_2$  electrolyser cell by switching between  $\text{CO}_2$  NTP and  $\text{CO}_2$  only at a current density of  $175 \text{ mA cm}^{-2}$ .



1 To decouple thermal effects from plasma-activated pathways, the impact of the feed  
2 gas temperature on cell voltage and product selectivity was evaluated (Fig. 4). Under  
3 the specific operating conditions ( $P_{\text{plasma}} = 10 \pm 0.5 \text{ W}$ ), the bulk temperature of the  
4  $\text{CO}_2$  NTP effluent was measured to be between 140–160 °C via external infrared  
5 thermometry.<sup>59, 60</sup> This range represents an upper bound, as the external positioning  
6 of the high-voltage electrode and comparison with higher power regimes (>16 W)  
7 suggest the internal gas temperature is likely lower.<sup>61</sup> Notably, gas heating in DBD is  
8 highly sensitive to reactor geometry, power density, and flow dynamics; thus, these  
9 values are specific to this architecture.<sup>60</sup> Galvanostatic  $\text{CO}_2$  RR (*i.e.* electrolysis) was  
10 performed at a current density of 175 mA cm<sup>-2</sup> for a duration of 1 hour to evaluate the  
11 influence of reactant activation modes. Three distinct experimental configurations  
12 were investigated: (1) ambient thermal control: plasma-off at 25 °C (or plasma  
13 deactivated), (2) elevated thermal control: plasma-off at 150 °C (to simulate plasma-  
14 induced heating), and (3) plasma-activated: plasma-on utilising a  $\text{CO}_2$  NTP DBD. The  
15 control experiment aimed to determine whether the product distribution observed  
16 during plasma-on operation stems from vibrationally or electronically excited  $\text{CO}_2$   
17 species rather than purely thermal effects.

18 To ensure a rigorous comparison of activation mechanisms, all experiments utilised  
19 identical electrolyte compositions, electrocatalysts, and ion-exchange membranes,  
20 thereby isolating the effects of reactant excitation from electrochemical cell variables.  
21 The performance of the electrolyte-gap electrolyser at a constant current density of  
22 175 mA cm<sup>-2</sup> is presented in Fig. 4. Under plasma-off conditions at 25 °C, the cell  
23 voltage stabilised at 4.48 V following a brief induction period of approximately 1.5–2 s  
24 (Fig. 4(a), red trace). This was followed by a subtle, continuous decline to ca. 4.45 V  
25 over a 2600 s period. While temperature is known to influence  $\text{CO}_2$  solubility, mass  
26 transport, and reaction thermodynamics,<sup>21, 62</sup> our results show that increasing the  $\text{CO}_2$   
27 feed temperature from 25 °C to 150 °C (plasma-off) at a current density of 175 mA cm<sup>-2</sup>  
28 resulted in only a negligible voltage decrease (from approximately 4.37 V at 25 °C  
29 to ~ 4.15 V at 150 °C, Fig. 4(a) purple line). In contrast, operation in plasma-on mode  
30 (Fig. 4 (a) black trace) resulted in a substantial reduction in cell voltage to 3.1 V. This  
31 potential remained highly stable throughout the 1-hour electrolysis period,  
32 representing a voltage saving of ~1.35 V compared to the conventional molecular  $\text{CO}_2$   
33 feed. The absence of significant voltage drift in the plasma-on mode suggests that the



1 activation of the reactant feed may also assist in maintaining steady-state conditions  
2 at the electrode-electrolyte interface.

3 Furthermore, the product distribution resulting from ambient thermal control, *that is*,  
4 plasma-off at 25 °C and elevated thermal control, *that is*, plasma-off at 150 °C  
5 (comprising H<sub>2</sub>, CO, CH<sub>4</sub>, C<sub>2</sub>H<sub>4</sub>, C<sub>2</sub>H<sub>5</sub>OH, and HCOO<sup>-</sup>), remained largely unchanged,  
6 with only a marginal increase in total FE by increasing the temperature of the CO<sub>2</sub>  
7 feed, as shown in Fig. 4(b). Conversely, we observed a transition toward C<sub>2</sub> and C<sub>3</sub>  
8 products upon integrating the CO<sub>2</sub> NTP DBD source with the electrochemical CO<sub>2</sub>RR,  
9 as illustrated in Fig. 4(b).

10 The limited impact of preheating the CO<sub>2</sub> feed to 150 °C confirms that the  
11 enhancements observed during the plasma-on mode are not primarily driven by  
12 thermal energy. This highlights the non-thermal advantages of the plasma, in which  
13 energetic electrons and reactive species (*e.g.*, O<sup>-</sup>, CO<sup>+</sup>) facilitate CO<sub>2</sub> dissociation or  
14 stabilise intermediates for C–C coupling.<sup>55, 63</sup> While OES confirmed the presence of  
15 radical species, a portion of the selectivity shift may arise from the modified feed  
16 composition (*i.e.*, CO/CO<sub>2</sub> mixtures generated *in situ*). Future studies utilising synthetic  
17 CO/CO<sub>2</sub>/He blends are required to precisely quantify the synergy between non-  
18 thermal excited species and CO co-feeding.

19



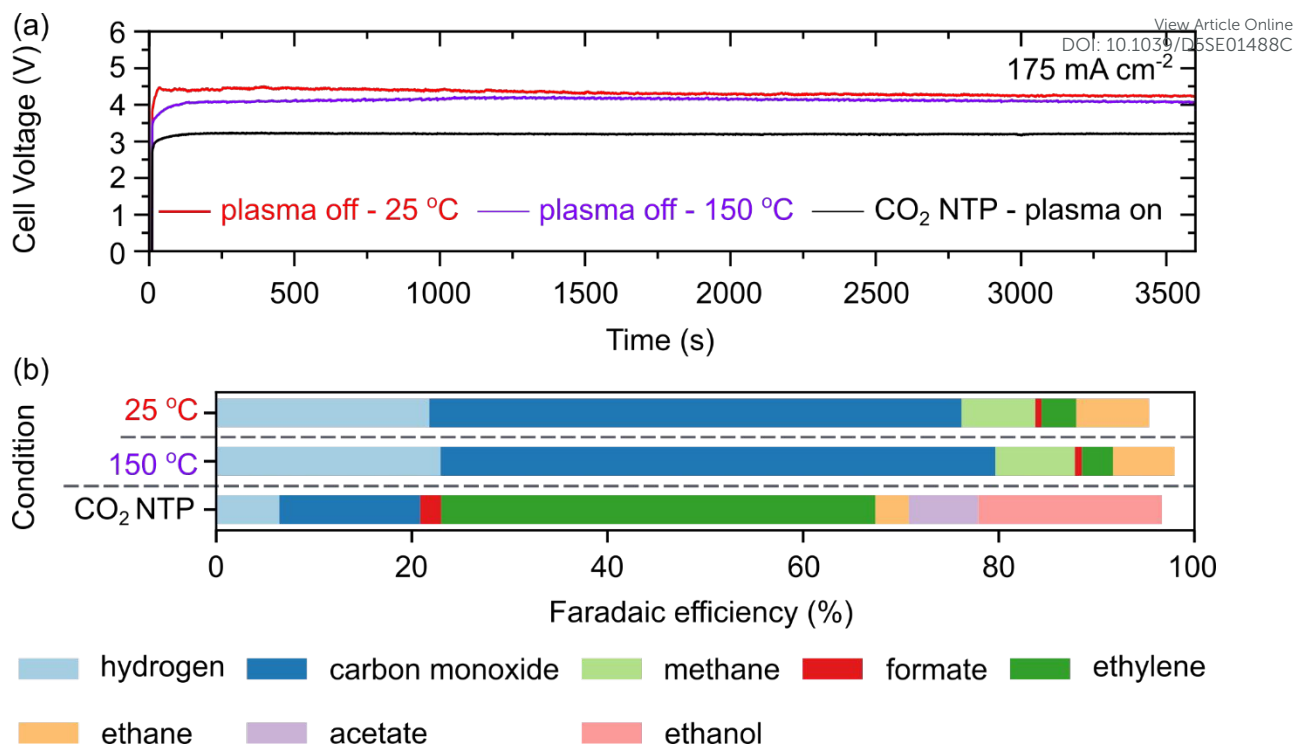


**Figure 4:** Comparative performance of electrochemical CO<sub>2</sub> conversion under non-thermal, thermal, and plasma-activated conditions. Galvanostatic experiments were carried out at 175 mA cm<sup>-2</sup> using the electrolyte-gap electrolyser and 0.5 M CsHCO<sub>3</sub> + 0.25 M Cs(SO<sub>3</sub>CH<sub>3</sub>) + 0.25 M Cs<sub>2</sub>SO<sub>4</sub> aqueous electrolyte. (a) Chronopotentiogram of CO<sub>2</sub> electrolysis using CO<sub>2</sub> gas at 25 °C (red line), 150 °C (purple line), and CO<sub>2</sub> NTP (black line) as the reactant source. (b) Corresponding FE of the products obtained.

To investigate the product distribution, the FE was monitored at 600-s intervals throughout the 1-hour electrolysis to assess the impact of reactant activation on product selectivity (Fig. 5). Notable shifts in the catalytic pathways were observed between the two operational modes. Under plasma-off conditions (Fig. 5(a)), the system predominantly produced C1 gaseous species, with carbon monoxide as the major product (FE = 54.6% ± 1.3), accompanied by methane (FE = 7.4% ± 0.76) and significant competitive HER (hydrogen FE = 26.1% ± 1.5). Small quantities of ethylene were also detected (FE = 3.55% ± 0.6). In contrast, the introduction of CO<sub>2</sub> NTP-DBD activation (Fig. 5(b)) fundamentally redirected the reaction toward C2+ pathways and suppressed the HER, with the hydrogen FE decreasing to 6.4% ± 1.25. Plasma-on operation promoted the formation of both gaseous and liquid multicarbon products. In



1 the gaseous phase, we noticed significant enhancement in ethylene (FE = 44.31% ±  
2 1.98) and the emergence of ethane (3.44% ± 0.57), while CO production was reduced  
3 to 14.5% ± 1.4. From the liquid phase, we recorded the production of ethanol (18.83%  
4 ± 1.3), acetate (7.14% ± 0.65), and formate (2.15% ± 0.55). The transition from a C1  
5 dominant regime to a combined gaseous/liquid C2+ distribution (total C2+ FE  
6 exceeding 70%) emphasises the advantage of plasma-assisted electrochemical CO<sub>2</sub>  
7 reduction. This selectivity shift is attributed to the presence of plasma-generated  
8 reactive species and vibrationally excited CO<sub>2</sub>, which likely lower the kinetic barriers  
9 for carbon–carbon coupling and stabilise key surface intermediates, thereby  
10 bypassing conventional scaling relationships that typically limit C1 to C2+ conversion.  
11 The results accentuate the non-thermal nature of CO<sub>2</sub> plasma benefits, where  
12 energetic electrons and reactive species (e.g., O<sup>-</sup>, CO<sup>+</sup>) directly participate in breaking  
13 CO<sub>2</sub> bonds or stabilising intermediates that facilitate C-C coupling,<sup>56, 63, 64</sup> potentially  
14 leading to non-explored CO<sub>2</sub> conversion pathways.

15 Despite the presence of high-energy electrons, ions, and reactive oxygen species  
16 (ROS) within the CO<sub>2</sub> NTP, the electrode showed no signs of significant delamination,  
17 sintering, or mechanical degradation, as shown in Fig. S13. The porous structure of  
18 the GDE, which is essential for efficient gas transport and maintenance of the triple-  
19 phase boundary, was preserved throughout the electrolysis period. Based on the  
20 experimental results, we drew the following observations regarding the electrode  
21 resilience. First, we discussed the thermal stability, in which the “non-thermal” nature,  
22 despite the involvement of high-energy species in the NTP, ensured that the bulk gas  
23 temperature remained relatively low, thereby preventing thermal damage to the PTFE  
24 binder or the carbon support within the GDE. Second, we tested the chemical  
25 robustness. Although the catalyst surface may undergo transient oxidation state  
26 changes (Cu<sup>0</sup> to Cu<sup>δ+</sup>) due to plasma-derived oxygen species, it did not exhibit  
27 irreversible poisoning or phase transformation that would inhibit CO<sub>2</sub> reduction  
28 kinetics. Third, we tested the catalyst adhesion, in which there was no evidence of  
29 catalyst “wash-off” into the catholyte, indicating that the plasma-on conditions did not  
30 compromise the interfacial bonding between the CuO nanoparticles and the gas  
31 diffusion layer. This demonstrated stability over one hour of continuous operation,  
32 suggesting that the plasma–electrochemical interface was robust enough for extended  
33 durability testing and potential scaling.



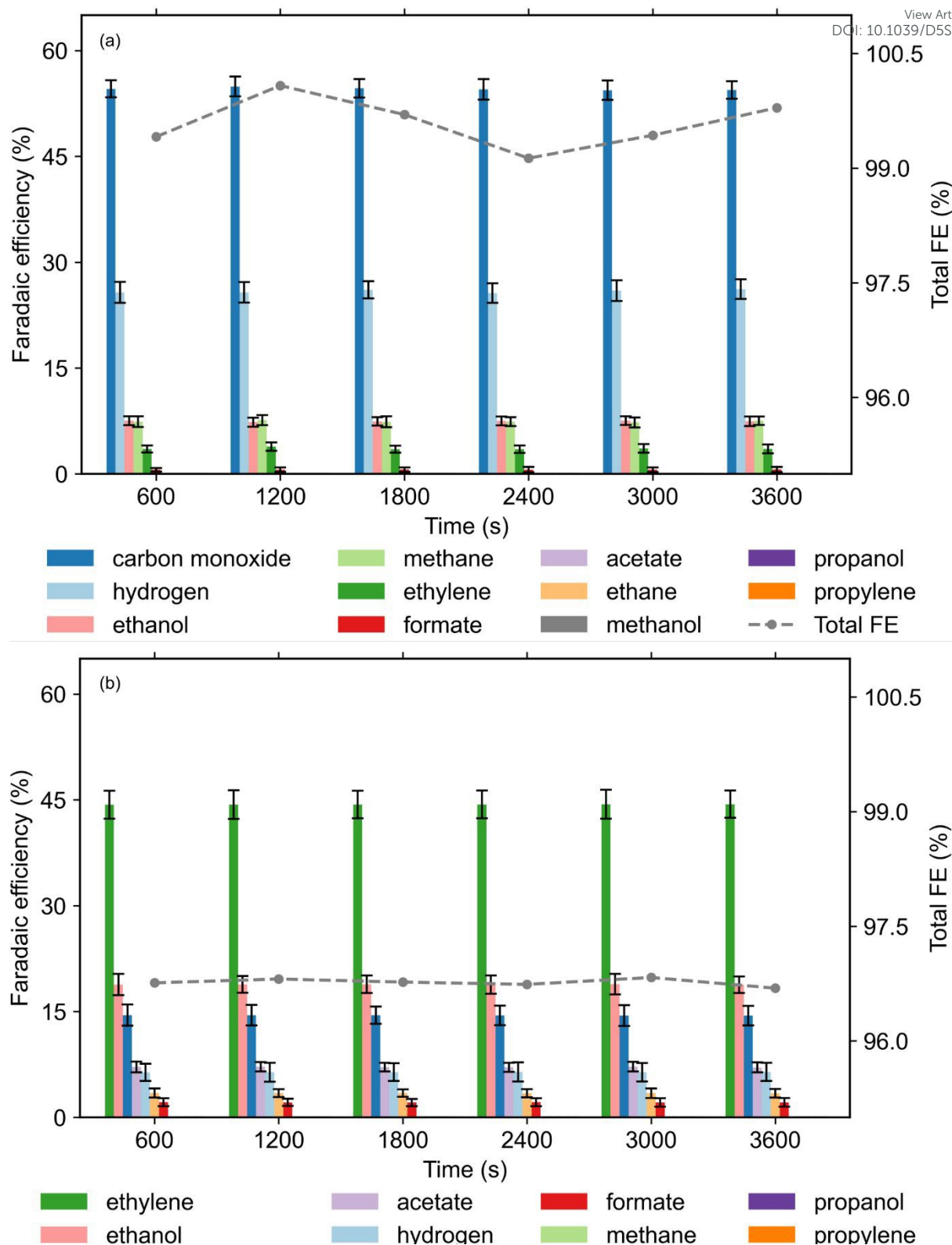


**Figure 5:** Comparative FE for electrochemical CO<sub>2</sub> conversion at 175 mA cm<sup>-2</sup> over 1 hour of electrolysis. (a) Product distribution under plasma-off conditions. (b) Product distribution under CO<sub>2</sub> NTP-DBD *i.e.* plasma-on conditions, demonstrates a strategic shift toward multicarbon gaseous and liquid products. Error bars represent the standard deviation (n=3) calculated from GC and HPLC measurements sampled at 600 s intervals.



1 Galvanostatic electrochemical CO<sub>2</sub>RR was performed at current densities ( $j$ ) ranging  
2 from 100 to 225 mA cm<sup>-2</sup> for 1 hour to evaluate the impact of plasma activation  
3 (plasma-on vs. plasma-off). Detailed results across the full current range are provided  
4 in the SI (Figs. S8–S12) and the corresponding cell voltage at each current density is  
5 shown in Fig. 6(a). Plasma-on operation consistently yielded lower cell voltages than  
6 plasma-off conditions across the entire current density range. For instance, at  $j = 100$   
7 mA cm<sup>-2</sup>, the cell voltage decreased from 3.45 V (plasma-off) to 2.60 V (plasma-on),  
8 representing a potential reduction  $|\Delta E| = E_{\text{plasma-off}} - E_{\text{plasma-on}} = 0.84$  V. This voltage  
9 gap widened significantly with increasing  $j$ , reaching a maximum difference of 2.03 V  
10 at 225 mA cm<sup>-2</sup> ( $E_{\text{plasma-off}} = 5.53$  V vs.  $E_{\text{plasma-on}} = 3.50$  V). This substantial reduction  
11 in overpotential suggests that the introduction of reactive plasma-generated species  
12 lowers the kinetic barriers for charge transfer at the electrode–electrolyte interface.<sup>65,</sup>  
13 <sup>66</sup> The cumulative FE for C1–C3 species is illustrated in Fig. 6 (b and c). The FE for  
14 C2 products (ethylene and ethanol) was maximised at lower current densities (100–  
15 150 mA cm<sup>-2</sup>) under plasma-on conditions (Fig. 6 (b and c)). Notably, the plasma-on  
16 mode facilitated the production of C3 species—specifically propylene and 1-propanol,  
17 which were absent during plasma-off experiments. While conventional  
18 electrochemical CO<sub>2</sub>RR typically terminates at C2 intermediates,<sup>67–69</sup> the diversity of  
19 plasma-generated species (including CO molecules, ions, and excited-state  
20 intermediates) likely facilitates chain propagation. The emergence of propylene (FE ~  
21 3.95%) and 1-propanol at 200 mA cm<sup>-2</sup> supports a plasma-mediated chain propagation  
22 mechanism.<sup>67</sup> It is hypothesised that the stabilisation of \*CH<sub>2</sub> intermediates on  
23 asymmetric CuO sites promotes C–C coupling with \*CO to form C3 precursors.<sup>56, 68, 70</sup>  
24 Comparative analysis highlights two critical advantages of plasma-integrated  
25 electrolysis: (1) enhanced cell voltage: the reactive nature of the plasma medium  
26 consistently lowers the operating cell voltage, a phenomenon attributed to the pre-  
27 activation of CO<sub>2</sub> molecules. (2) Product selectivity: plasma-on operation shifts the  
28 selectivity from primary syngas components (CO and H<sub>2</sub>) toward high-value C2+  
29 products. This is evidenced by the higher FE for ethylene and the unique synthesis of  
30 C3 hydrocarbons and alcohols, indicating a fundamental change in the reaction  
31 pathway mediated by plasma-generated intermediates.



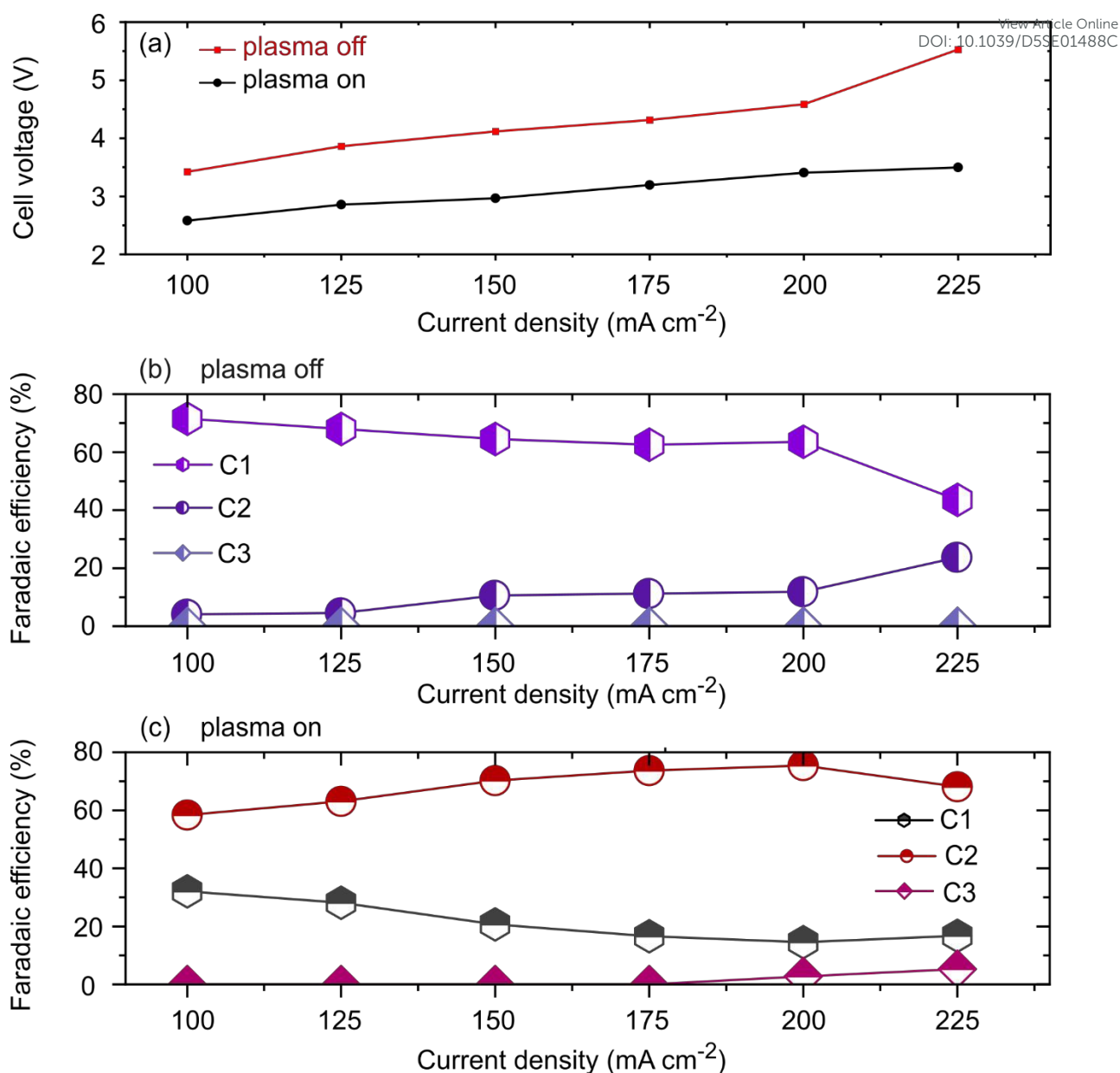


**Figure 6:** Performance and selectivity of plasma-integrated electrochemical CO<sub>2</sub> reduction (a) Cell voltage as a function of current density for plasma-off (red line) and plasma-on (black line) conditions across varying current densities (100–225 mA cm<sup>-2</sup>). FE for gaseous products and liquid products (b) plasma-off and (c) plasma-on.

1

2 The dependence of the gaseous and liquid product FE on  $j$  is summarised in Fig. 7(a–  
 3 d). Under plasma-off conditions (Fig. 7a and b), CO was the primary gaseous product,  
 4 although its FE declined from 64.74% at 100 mA cm<sup>-2</sup> to 34.73% at 225 mA cm<sup>-2</sup>. This  
 5 downward trend in FE<sub>CO</sub> was particularly pronounced at  $j > 150$  mA cm<sup>-2</sup>, correlating  
 6 with increased competitive HER and the onset of liquid product formation. Specifically,  
 7 ethanol and formate production commenced at 150 mA cm<sup>-2</sup> (FE of 6.59% and 0.51%,



1 respectively), with ethanol reaching a maximum FE of 22.12% at the highest current  
2 density. Methane production peaked at 200 mA cm<sup>-2</sup> (FE = 8.85%), at which point  
3 ethylene selectivity was suppressed to its minimum (FE = 2.48%), suggesting a shift  
4 in intermediate pathways at high overpotentials.

5 Activation of the CO<sub>2</sub> plasma significantly diversified the product profile (Fig. 7c, d).  
6 The gas phase included ethane, ethylene, and propylene, whereas the liquid phase  
7 contained formate, acetate, ethanol, and 1-propanol. Notably, the introduction of  
8 plasma suppressed methane formation to non-detectable levels and stabilised the FE  
9 of H<sub>2</sub> at an average of ~6.5%. Despite CO being the primary species generated within  
10 the CO<sub>2</sub> NTP,<sup>50, 52, 71, 72</sup> its FE decreased as *j* increased. This was mirrored by a  
11 substantial increase in ethylene selectivity, which reached 45.89% at 225 mA cm<sup>-2</sup>.  
12 This observation is consistent with the literature suggesting that plasma-generated CO  
13 serves as a high-concentration reactant that is more readily reduced to C<sub>2</sub><sup>+</sup> species  
14 than molecular CO<sub>2</sub>.<sup>73, 74</sup>

15 The plasma-on system uniquely facilitated the synthesis of C<sub>3</sub> products. Propylene  
16 production was initiated at 200 mA cm<sup>-2</sup>, reaching a maximum FE of 3.95% at 225 mA  
17 cm<sup>-2</sup>. Similarly, 1-propanol was detected at higher current densities, peaking at 225  
18 mA cm<sup>-2</sup>, reaching an FE of 1.28%. In the liquid phase, ethanol remained the dominant  
19 product under plasma-on conditions, achieving a maximum FE of 21.69% at a  
20 relatively low current density of 150 mA cm<sup>-2</sup>. The transition from formate (maximum  
21 FE 8.41% at 100 mA cm<sup>-2</sup>) to acetate (maximum FE 7.29% at 225 mA cm<sup>-2</sup>) further  
22 indicates that plasma-mediated species enhance C-C coupling by stabilising \*CH<sub>2</sub>  
23 intermediates on asymmetric CuO sites and chain elongation pathways via \*CH<sub>2</sub>  
24 intermediates that are inaccessible in conventional electrochemical systems.<sup>35, 75</sup>

25

26

27



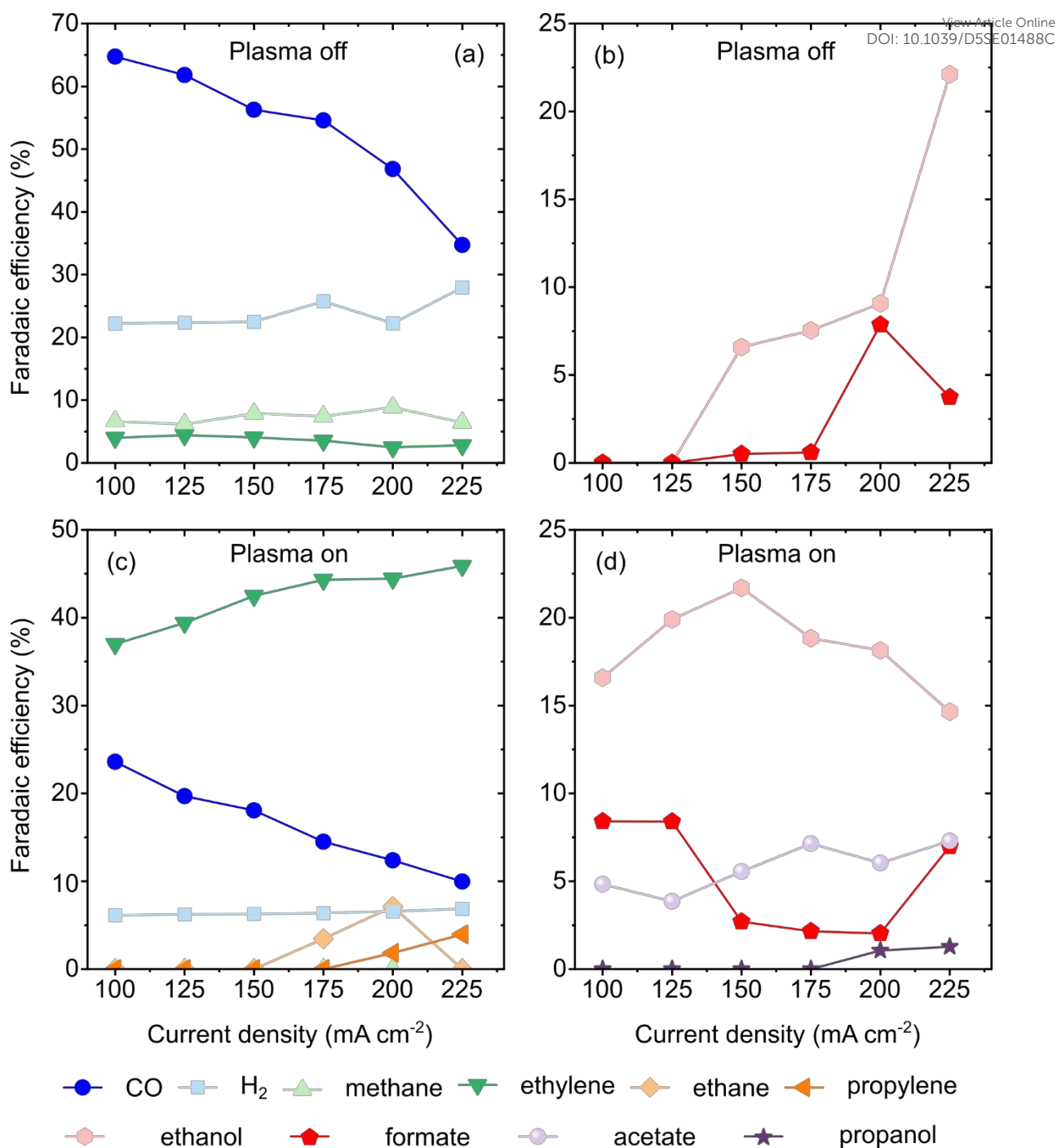


**Figure 7:** Plasma-off (a and b) and plasma-on (c and d) FEs of CO<sub>2</sub> conversion to gas (a and c) and liquid (b and d) products as a function of the current density.

1

2 Assessing the energy efficiency (*EE*) of electrochemical CO<sub>2</sub>RR, DBD NTP  
 3 generation, and hybrid DBD-assisted CO<sub>2</sub> electrolysis is essential, as these electricity-  
 4 driven processes exhibit distinct thermodynamic losses and downstream  
 5 requirements. For CO<sub>2</sub>RR, performance benchmarking incorporates FE, *j*, and cell  
 6 voltage into a comprehensive electrical-to-chemical efficiency metric (*EE* =



1  $(FE \times \Delta V_{\text{thermodynamic}}) / \Delta V_{\text{cell}}$ ). Techno-economic viability generally necessitates  
 2  $j \geq 100 - 200 \text{ mA cm}^{-2}$  and  $EE \geq 50\%$ , with explicit reporting of carbon conversion  
 3 efficiency to accurately reflect reactant utilisation.<sup>58</sup> The architecture of the reactor  
 4 further influences these metrics; for example, GDE configurations in acidic media can  
 5 enhance  $EE$  by  $\sim 30\%$  relative to neutral electrolytes by mitigating carbonate-related  
 6 penalties.<sup>76</sup> Conversely, the performance of DBD is determined by the specific energy  
 7 input (SEI), which inherently involves a trade-off with  $\text{CO}_2$  conversion ( $X_{\text{CO}_2}$ ) and  
 8 energy efficiency ( $\eta$ ) *i.e.* the efficiency of utilising the plasma energy for the chemical  
 9 conversion.<sup>77</sup> Exemplary values range from  $\eta \approx 9.4\%$  at  $X_{\text{CO}_2} \approx 4.2\%$  ( $\text{SEI} \approx 25 \text{ kJ L}^{-1}$ )  
 10 to  $\eta \approx 94.1\%$  at  $X_{\text{CO}_2} \approx 51\%$  ( $\text{SEI} \approx 155 \text{ kJ L}^{-1}$ ).<sup>77</sup>

11 The integration of  $\text{CO}_2$  plasma with electrochemical  $\text{CO}_2$  reduction significantly alters  
 12 the product distribution and the  $EE$  across a range of current densities, as illustrated  
 13 in Fig. 8 and S5, Fig. S14 and Equations S6-S8. An  $EE_{\text{CO}}$  of 25.35% was achieved  
 14 when the cell was operated under plasma-off conditions at a current density of  
 15  $100 \text{ mA cm}^{-2}$ . The  $EE_{\text{CO}}$  decreases with increasing current density, reaching a  
 16 minimum value of 8.41% at a current density of  $225 \text{ mA cm}^{-2}$ . Methane was only  
 17 produced under the plasma-off mode and reached a peak  $EE_{\text{methane}}$  value of 2.85% at  
 18  $100 \text{ mA cm}^{-2}$  and a minimum  $EE_{\text{methane}}$  value of 1.70% at  $225 \text{ mA cm}^{-2}$ . The  $EE_{\text{ethylene}}$   
 19 gradually decreases with increasing current density, reaching a value of 1.84% at  
 20  $100 \text{ mA cm}^{-2}$  and a minimum of 0.8% at  $225 \text{ mA cm}^{-2}$ . This observation of the highest  
 21 and lowest  $EE_{\text{methane}}$  and  $EE_{\text{ethylene}}$  values is associated with the production of liquid  
 22 products, specifically formate and ethanol, where formate (C1 product) achieved the  
 23 highest  $EE_{\text{formate}}$  of 3.15% at  $200 \text{ mA cm}^{-2}$ , and ethanol (C2 product) the highest  
 24  $EE_{\text{ethanol}}$  of 6.24% at  $225 \text{ mA cm}^{-2}$ . In general, under plasma-off conditions, the  $EE$  is  
 25 predominantly concentrated in simpler products, with CO being the most significant.  
 26 Methane and ethylene reached an  $EE$  between 0.5% and 3% across the applied  
 27 current density range. Ethanol and formate were observed when current densities  
 28 above  $150 \text{ mA cm}^{-2}$  were applied. This implies that, in the absence of plasma, the  
 29 system favours C1 products ( $\text{CO}$ ,  $\text{CH}_4$ ) with limited formation of multi-carbon (C2)  
 30 products (see also Fig. 6(b)).

31 As shown in Fig. 8(b), although plasma-on experiments lead to valuable C2+ products,  
 32 this is at the expense of a much lower  $EE$ , both overall and for each product.  $EE_{\text{CO}}$



1 decreases with increasing current density, while  $EE_{\text{formate}}$  first shows a high  $EE_{\text{formate}}$   
2 of 1.65% at 100 mA cm<sup>-2</sup>, then decreases when the current is increased, and reaches  
3 a minimum  $EE_{\text{formate}}$  of 0.24% at 200 mA cm<sup>-2</sup>. This coincides with the emergence of  
4 various C2 and C3 products, mainly liquid C3 products. Despite this trend,  $EE_{\text{formate}}$   
5 increases when 225 mA cm<sup>-2</sup> is applied and reaches 0.82%.  $EE_{\text{ethylene}}$  shows a slight  
6 change during the investigated current densities (100–225 mA cm<sup>-2</sup>), from  $EE_{\text{ethylene}}$  of  
7 0.51% at 100 mA cm<sup>-2</sup> to  $EE_{\text{ethylene}}$  of 0.48% at 225 mA cm<sup>-2</sup>.  $EE_{\text{ethanol}}$  exhibits a  
8 volcano trend with a maximum of 0.66% at 150 mA cm<sup>-2</sup>, and  $EE_{\text{ethane}}$  reaches a  
9 maximum of 0.015% at 200 mA cm<sup>-2</sup>.  $EE_{\text{acetate}}$  presents an erratic response with  
10 current density, reaching a maximum of 0.51% at 175 mA cm<sup>-2</sup>.

11 As sustained  $FE$  gains are achieved,  $EE_{\text{propylene}}$  and  $EE_{\text{propanol}}$  (C3 products produced  
12 solely under plasma-on conditions) increase with increasing current density. Both  
13 reached their maximum  $EE$  values of 0.02% and 0.018%, respectively, at 225 mA cm<sup>-2</sup>.  
14 The observed reduction in  $EE$  during plasma-on operation can be attributed to the  
15 incomplete coupling between the discharge and the catalytic interface. This is due to  
16 the separation of the discharge zone from the cathode by post-discharge transport,  
17 characterised by a rod tip-to-cathode distance of 10 mm. This separation and  
18 convection following discharge allow time for the plasma species to relax or  
19 recombine. CO and O recombine to form CO<sub>2</sub>, resulting in a loss of conversion  
20 achieved within the plasma,<sup>60, 61</sup> or return to the ground state through energy-  
21 relaxation processes before reaching the catalyst, an effect that is likely intensified by  
22 the presence of the GDE.<sup>59, 60</sup> This results in the power deposited in the plasma not  
23 being utilised effectively, with the effect being variable depending on the lifetime of all  
24 plasma species.<sup>59, 60</sup> Some of these, such as the radicals and vibrationally excited  
25 states, have relatively long lifetimes, whereas others, such as ions and electronically  
26 excited states, have much shorter lifetimes.<sup>54, 55, 57, 63, 67, 70, 78</sup> The species that reach  
27 the catalyst surface likely drive the conversion process. To enhance  $EE$ , it is  
28 anticipated that reducing post-discharge transport losses, such as by decreasing the  
29 discharge-to-GDE distance and minimising dead volume, optimising the flow rate to  
30 increase the proportion of activated species reaching the interface, and/or integrating  
31 the discharge closer to the GDE plane, will be necessary.



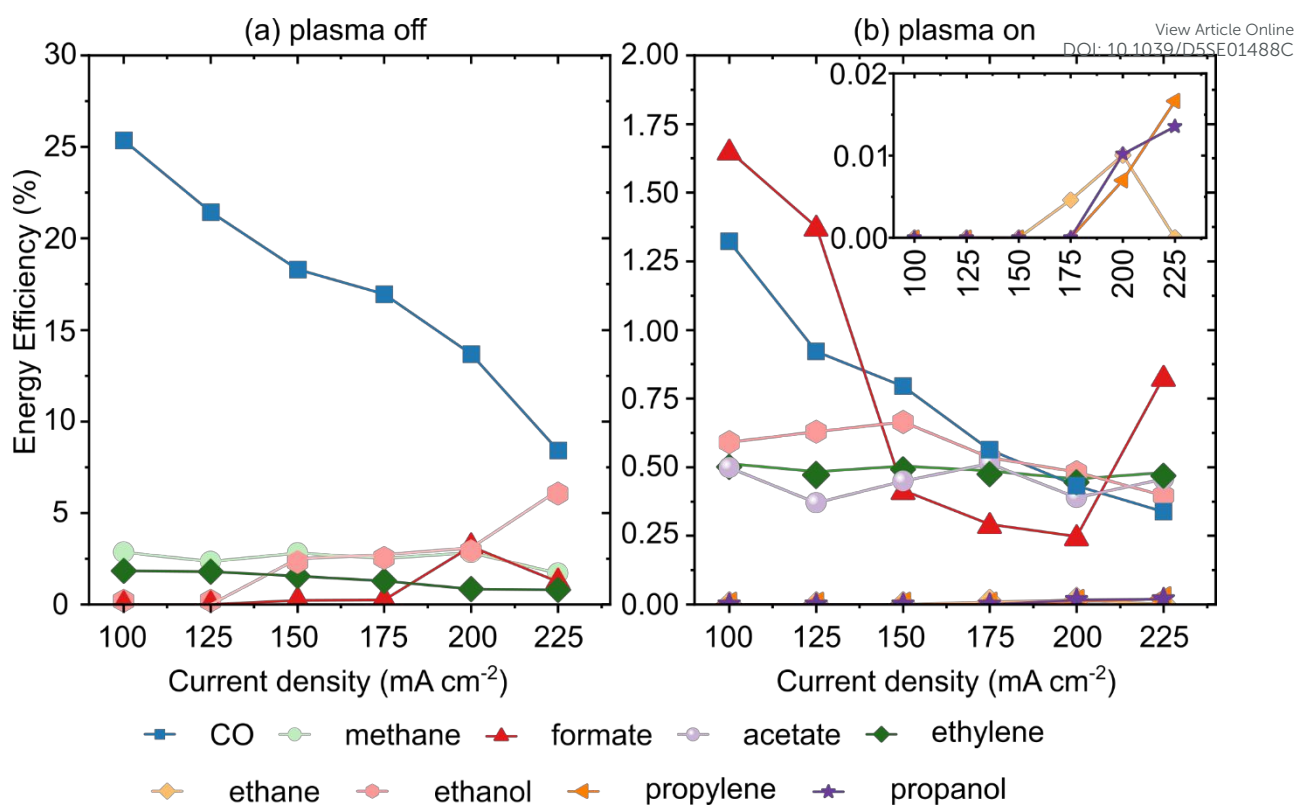


**Figure 8:** (a) Plasma-off and (b) plasma-on energy efficiency for gases and liquid products vs current density.

The analysis of carbon efficiency (%), as depicted in Fig. 9 and S6-S9, Tables S3-S8, evaluates the carbon yield ( $Y_{\text{carbon}}$ ), which is defined as the percentage of the total  $\text{CO}_2$  feed converted into detectable gaseous and liquid products. The carbon efficiency (%) or yield for the sum of gas, liquid, and carbonate products ranged from 1.86% to 2.47% under plasma-off conditions and from 1.33% to 2.45% under plasma-on conditions (S9, Table S8). The remaining carbon yield predominantly consists of unreacted  $\text{CO}_2$  (~75% plasma off and ~80% plasma on) exiting the gas stream. This may stem from a GDE-based flow cells operating at high volumetric flow rates to mitigate mass transport limitations, and inorganic carbon species sequestered in the electrolyte. Plasma activation induces a distinct shift in carbon distribution. In the gas-phase and under plasma-off conditions, the gas-phase carbon efficiency is higher (1.71–2.12%) compared to plasma-on operation (0.91–1.52%) across the tested current densities (Table S3). This observation aligns with the predominant production of CO via the conventional  $2e^-$  reduction pathway when the plasma is inactive. Conversely, in the liquid-phase, plasma activation significantly enhances liquid-phase carbon incorporation (Table S4). Notable production of C2 and C3 oxygenates (ethanol,



1 propanol, acetate) were observed at low current densities (e.g., 0.41% yield at 100  
2 mA cm<sup>-2</sup>), whereas liquid product formation was negligible under plasma-off conditions  
3 until 150 mA cm<sup>-2</sup>. At 225 mA cm<sup>-2</sup>, the reduction in gas-phase yield under plasma-on  
4 conditions (1.52% vs 2.12% for plasma-off) correlates with the diversion of carbon flux  
5 toward higher-order liquid products (liquid yield for plasma on is 0.91% vs 0.63% for  
6 plasma off), confirming that plasma species facilitate chain growth over simple  
7 desorption as CO. In terms of inorganic carbon sequestration, we registered the  
8 formation of inorganic carbon byproducts (carbonate and bicarbonate) which acts as  
9 a parasitic sink for the CO<sub>2</sub> feed. This sequestration was consistently higher under  
10 plasma-off conditions (0.011-0.027%) compared to plasma-on (0.01-0.022%). This  
11 difference is mechanistically linked to the interfacial pH environment. As detailed in  
12 Tables S6-S7, plasma-off operation resulted in a highly alkaline effluent (pH 8.2–11.3),  
13 which shifts the equilibrium toward rapid CO<sub>2</sub> neutralisation:  $\text{CO}_2 + 2\text{OH}^- \rightarrow \text{CO}_3^{2-} + \text{H}_2\text{O}$ .  
14 This will result in increased crossover of carbon towards the anode and increased  
15 inorganic carbon reservoirs, such as membrane-stored carbonate, within the reactor.  
16 In contrast, the plasma-on mode maintained a more moderate pH (7.5–9.2), due to  
17 the formation of formate and acetate, which consume  $n - 1$  protons per  $n$  electrons  
18 transferred. Consequently, plasma-on operation results in a smaller pH increase and  
19 less carbonate formation, thereby preserving a slightly larger fraction of the dissolved  
20 inorganic carbon for electrochemical conversion into high-value C2 and C3 fuels.

View Article Online  
DOI: 10.1039/D5SE01488C



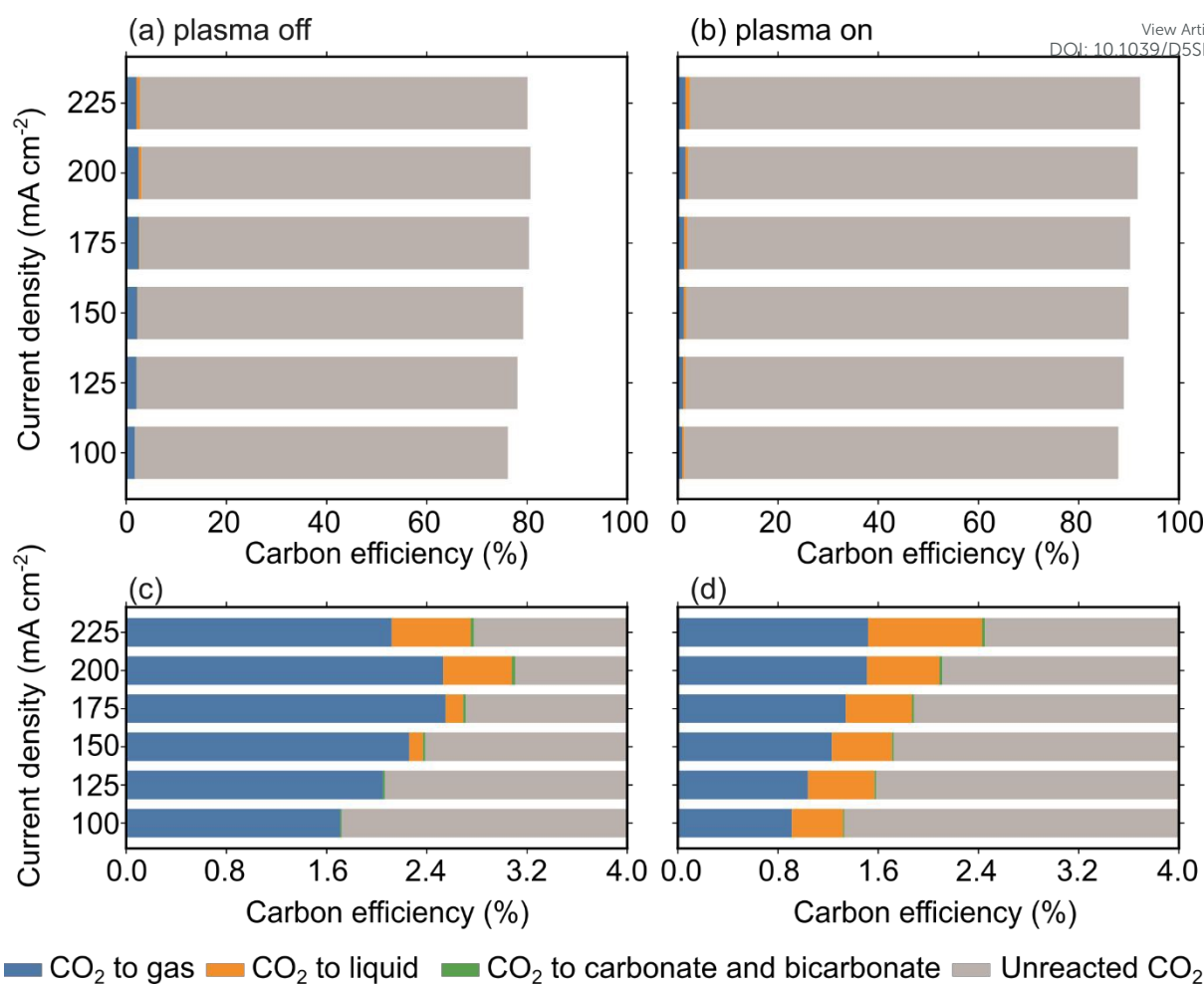


**Figure 9:** Carbon efficiency (yield) for the conversion of CO<sub>2</sub> to gas, liquid, carbonate, and bicarbonate under (a and c) plasma off and (b and d) plasma on modes, c and d are zoom in plots.

1

2 The results illustrate that plasma activation effectively suppresses HER, with the FE  
 3 for H<sub>2</sub> decreasing from 22.2% (plasma-off) to 6.2% (plasma-on). This shift facilitates  
 4 the redirection of the electron flux toward CO<sub>2</sub> reduction, thereby significantly  
 5 enhancing the selectivity for C<sub>2</sub> products. Specifically, the FE for ethylene increased  
 6 from 3.2% to 40.5%, while ethanol production, undetectable under plasma-off  
 7 conditions, reached an FE of 20.1%.

8 The CO<sub>2</sub> NTP DBD generates a diverse population of reactive species, including ions  
 9 (CO<sub>2</sub><sup>+</sup>, CO<sup>+</sup>), molecules, excited states, radicals, and vibrationally or electronically  
 10 excited states (CO<sub>2</sub><sup>\*</sup>, CO<sup>\*</sup>).<sup>38</sup> The synergetic coupling of the CO<sub>2</sub> NTP DBD with  
 11 electrochemical reduction induces a fundamental shift in both the energetic and kinetic



1 landscapes of the reaction, beyond the substantial reduction in cell voltage. While CO  
2 and vibrationally excited CO<sub>2</sub> serve as primary reactive precursors for C<sub>2</sub>+  
3 synthesis,<sup>57, 58, 67, 70, 72, 79</sup> the concomitant generation of oxygen-bearing species (O,  
4 O<sub>2</sub>, O<sub>3</sub>) may play a role in the product distribution. These species potentially stabilise  
5 catalytic Cu<sup>δ+</sup> moieties, known to promote C–C coupling by modifying CO adsorption  
6 energies,<sup>6, 34, 35, 66, 67, 80</sup> although their reduction may simultaneously detract from  
7 overall EE. Collectively, these results suggest that the enhanced selectivity toward  
8 high-value C<sub>2</sub>+ products is a result of a multi-component synergy involving plasma-  
9 activated carbon species and transient oxygen-driven surface stabilisation of Cu<sup>δ+</sup>  
10 species.

11 Interestingly, the plasma-on mode exhibits an attenuated local pH compared to  
12 plasma-off operation. This is attributed to the stoichiometric shift in product selectivity.  
13 The synthesis of carboxylates such as formate and acetate requires  $n - 1$  protons per  
14  $n$  transferred electrons, while all the other products (e.g. CO, methane, ethanol)  
15 consume the same number of electrons and protons. Consequently, the plasma-  
16 mediated pathway reduces the interfacial proton demand and leads to a smaller pH  
17 increase.

18 Notably, a reduction in cell voltage was observed during plasma-on operation, where  
19 an average decrease of  $\sim 1.3$  V was attributed to two factors. First, the partial provision  
20 of the Gibbs free energy ( $\Delta G$ ) required for CO<sub>2</sub> reduction during the plasma excitation  
21 phase. Second, the emergence of alternative reaction pathways with lower activation  
22 energies ( $E_{\text{activation}}$ ) for the reduction of plasma-activated species.

23 Mechanistically, the formation of propylene (FE 3.95%) alongside ethylene (FE  
24 45.89%) suggests a coupling pathway between C<sub>2</sub> intermediates and CO<sub>2</sub>-derived  
25 radicals or carboxyl species (\*COOH). At higher current densities (e.g., 200 and 225  
26 mA cm<sup>-2</sup>), increased product diversity and C<sub>2</sub> selectivity are observed, likely driven  
27 by a combination of plasma-induced kinetic enhancements and local mass transport  
28 dynamics. Additionally, the plasma-on state lowers the interfacial pH, thereby  
29 mitigating carbonate formation and directing the carbon flux toward liquid products,  
30 such as acetate and propanol.

31 The higher pH reached in the catholyte with plasma off facilitates the neutralisation of  
32 CO<sub>2</sub> by OH<sup>-</sup>, resulting in the formation of HCO<sub>3</sub><sup>-</sup>/CO<sub>3</sub><sup>2-</sup>. This process consequently



1 enhances (bi)carbonate formation and diminishes the proportion of carbon available  
2 for product synthesis.

3 Despite the shift toward value-added products, the sum of carbon efficiency for both  
4 gas and liquid remained low (average of 2.5% for plasma off vs. average of 2% for  
5 plasma on). These losses are attributed to CO<sub>2</sub> crossover, dissolution in the  
6 electrolyte, or adsorption within the GDE. Furthermore, while the electrochemical cell  
7 voltage decreases, the overall system EE remains low due to the energy-intensive  
8 nature of DBD NTP and subsequent recombination reactions (*e.g.*, CO + O → CO<sub>2</sub>)  
9 occurring in the post-discharge zone. Nevertheless, this hybrid system demonstrates  
10 the capability for flexible product tuning and provides a scalable framework for  
11 sustainable carbon utilisation.

## 12 Conclusions

13 We herein demonstrate a system that integrates a CO<sub>2</sub> DBD-NTP source with an  
14 electrolyte-gap CO<sub>2</sub> electrolyser utilising CuO-based cathodes, thereby facilitating a  
15 direct comparison between plasma-on and plasma-off operations at current densities  
16 of 100–225 mA cm<sup>-2</sup>. Plasma-on operation consistently reduces the cell voltage and  
17 shifts product selectivity from C1-dominated products toward higher-value C2+  
18 products, such as ethylene, propylene, formate, and acetate. Carbon analysis reveals  
19 that plasma-on operation redistributes carbon away from (bi)carbonate formation  
20 toward gas and liquid products; although the overall carbon recovery remains modest,  
21 indicating the presence of substantial unquantified sinks typical of GDE CO<sub>2</sub>  
22 electrolysis. Although the current configuration is not energy-efficient when accounting  
23 for plasma power, the findings establish a proof-of-concept for utilising plasma-  
24 activated feeds to modulate CO<sub>2</sub>RR selectivity within a flow-cell architecture. Future  
25 research will focus on enhancing the plasma–electrode coupling through optimisation  
26 of the geometry and residence time, and isolating the role of oxygen species.

27

## 28 ASSOCIATED CONTENT

### 29 Supporting Information

30 Additional information, tables of results, and figures S1-S9 (PDF)



**1 AUTHOR INFORMATION****2 Corresponding Author****3 E-mail:****4 [p.kechagiopoulos@abdn.ac.uk](mailto:p.kechagiopoulos@abdn.ac.uk);****5 [angel.cuestaciscar@abdn.ac.uk](mailto:angel.cuestaciscar@abdn.ac.uk)****6 [acuesta@iqf.csic.es](mailto:acuesta@iqf.csic.es)****7 ORCID****8 Haytham E. M. Hussein: 0000-0002-5238-4590****9 Panagiotis N. Kechagiopoulos: 0000-0002-4575-694X****10 Angel Cuesta: 0000-0003-4243-1848****11 Author Contributions**

**12** H.E.M.H., P.N.K., and A.C. devised the concept of combined NTP-electrochemical  
**13** platforms for CO<sub>2</sub> electrochemical conversion and designed a hybrid device. H.E.M.H.  
**14** and P.N.K. performed the experiments. H.E.M.H. performed microscopy imaging.  
**15** H.E.M.H. prepared the substrates and electrochemical device. H.E.M.H. and P.N.K.  
**16** conducted the conversion experiments. H.E.M.H., P.N.K., and A.C. were involved in  
**17** the data analysis. H.E.M.H., P. N. K. and A. C. wrote the manuscript.

**18 Conflict of interest****19** The authors declare no conflicts of interest.**20 Acknowledgements**

**21** This work is part of the Electrocatalysis in Non-Thermal Plasma for Energy Storage  
**22** (COPLE) project funded by the Adventurous Energy Research for a Sustainable Net  
**23** Zero Programme Grant from the EPSRC (EP/X000931/1). All data supporting this



1 study are available from the University of Aberdeen Repository. The authors thank  
2 Jonathan Rose, Yaroslav Kruchek, Robert Skinner, Raymond Stephen, Jonathan  
3 Edwards, and Matthew Craib for their technical support.

[View Article Online](#)  
DOI: 10.1039/D5SE01488C

4  
5  
6  
7



1 **References**

- 2 1. S. Overa, B. H. Ko, Y. Zhao and F. Jiao, *Accounts of Chemical Research*, 2022,  
3 **55**, 638-648.
- 4 2. A. Dutta, M. Rahaman, M. Mohos, A. Zanetti and P. Broekmann, *ACS*  
5 *Catalysis*, 2017, **7**, 5431-5437.
- 6 3. W. Choi, Y. Choi, E. Choi, H. Yun, W. Jung, W. H. Lee, H. S. Oh, D. H. Won, J.  
7 Na and Y. J. Hwang, *Journal of Materials Chemistry A*, 2022, **10**, 10363-10372.
- 8 4. M. Lima, C. M. Godoi, M. C. L. Santos, J. Nandenha, A. O. Neto and R. F. B.  
9 De Souza, *International Journal of Hydrogen Energy*, 2022, **47**, 4010-4017.
- 10 5. Y. Hori, I. Takahashi, O. Koga and N. Hoshi, *The Journal of Physical Chemistry*  
11 *B*, 2002, **106**, 15-17.
- 12 6. M. Sassenburg, M. Kelly, S. Subramanian, W. A. Smith and T. Burdyny, *ACS*  
13 *Energy Lett*, 2023, **8**, 321-331.
- 14 7. L. Hoof, N. Thissen, K. Pellumbi, K. Junge Puring, D. Siegmund, A. K. Mechler  
15 and U.-P. Apfel, *Cell Reports Physical Science*, 2022, **3**.
- 16 8. A. Ozden, J. Li, S. Kandambeth, X. Y. Li, S. J. Liu, O. Shekhah, P. F. Ou, Y. Z.  
17 Finrock, Y. K. Wang, T. Alkayyali, F. P. G. de Arquer, V. S. Kale, P. M. Bhatt,  
18 A. H. Ip, M. Eddaoudi, E. H. Sargent and D. Sinton, *Nature Energy*, 2023, **8**,  
19 179-190.
- 20 9. W. C. Ma, S. J. Xie, T. T. Liu, Q. Y. Fan, J. Y. Ye, F. F. Sun, Z. Jiang, Q. H.  
21 Zhang, J. Cheng and Y. Wang, *Nature Catalysis*, 2020, **3**, 478-487.
- 22 10. J. Schneider, H. Jia, J. T. Muckerman and E. Fujita, *Chem Soc Rev*, 2012, **41**,  
23 2036-2051.
- 24 11. S. Zhang, P. Kang, M. Bakir, A. M. Lapidés, C. J. Dares and T. J. Meyer, *Proc*  
25 *Natl Acad Sci U S A*, 2015, **112**, 15809-15814.
- 26 12. B. A. W. Mowbray, D. J. Dvorak, N. Taherimakhsoosi and C. P. Berlinguette,  
27 *Energy & Fuels*, 2021, **35**, 19178-19184.
- 28 13. K. Qi, Y. Zhang, N. Onofrio, E. Petit, X. Cui, J. Ma, J. Fan, H. Wu, W. Wang, J.  
29 Li, J. Liu, Y. Zhang, Y. Wang, G. Jia, J. Wu, L. Lajaunie, C. Salameh and D.  
30 Voiry, *Nature Catalysis*, 2023, **6**, 319-331.
- 31 14. G. Marcandalli, A. Goyal and M. T. M. Koper, *ACS Catal*, 2021, **11**, 4936-4945.
- 32 15. M. Moura de Salles Pupo and R. Kortlever, *Chemphyschem : a European*  
33 *journal of chemical physics and physical chemistry*, 2019, **20**, 2926-2935.
- 34 16. S. Garg, Q. C. Xu, A. B. Moss, M. Mirolo, W. Y. Deng, I. Chorkendorff, J. Drnec  
35 and B. Seger, *Energy & Environmental Science*, 2023, **16**, 1631-1643.
- 36 17. Y. Zhao, L. Hao, A. Ozden, S. Liu, R. K. Miao, P. Ou, T. Alkayyali, S. Zhang, J.  
37 Ning, Y. Liang, Y. Xu, M. Fan, Y. Chen, J. E. Huang, K. Xie, J. Zhang, C. P.  
38 O'Brien, F. Li, E. H. Sargent and D. Sinton, *Nature Synthesis*, 2023, **2**, 403-  
39 412.
- 40 18. A. S. Varela, *Current Opinion in Green and Sustainable Chemistry*, 2020, **26**,  
41 100371.
- 42 19. X. Liu, P. Schlexer, J. Xiao, Y. Ji, L. Wang, R. B. Sandberg, M. Tang, K. S.  
43 Brown, H. Peng, S. Ringe, C. Hahn, T. F. Jaramillo, J. K. Nørskov and K. Chan,  
44 *Nature Communications*, 2019, **10**, 32.
- 45 20. M. C. O. Monteiro, A. Mirabal, L. Jacobse, K. Doblhoff-Dier, S. C. Barton and  
46 M. T. M. Koper, *JACS Au*, 2021, **1**, 1915-1924.
- 47 21. R. E. Vos, K. E. Kolmeijer, T. S. Jacobs, W. van der Stam, B. M. Weckhuysen  
48 and M. T. M. Koper, *ACS Catalysis*, 2023, **13**, 8080-8091.



- 1 22. Y. Pei, H. Zhong and F. Jin, *Energy Science & Engineering*, 2021, **9**, 1012. Open Access Article Online  
DOI: 10.1039/C5SE01488C
- 2 1032.
- 3 23. M. R. Gonçalves, A. Gomes, J. Condeço, R. Fernandes, T. Pardal, C. A. C.  
4 Sequeira and J. B. Branco, *Energy Conversion and Management*, 2010, **51**,  
5 30-32.
- 6 24. F.-Y. Gao, R.-C. Bao, M.-R. Gao and S.-H. Yu, *Journal of Materials Chemistry*  
7 *A*, 2020, **8**, 15458-15478.
- 8 25. D. R. Kauffman, J. Thakkar, R. Siva, C. Matranga, P. R. Ohodnicki, C. Zeng  
9 and R. Jin, *ACS applied materials & interfaces*, 2015, **7**, 15626-15632.
- 10 26. M. Zhong, K. Tran, Y. Min, C. Wang, Z. Wang, C.-T. Dinh, P. De Luna, Z. Yu,  
11 A. S. Rasouli, P. Brodersen, S. Sun, O. Voznyy, C.-S. Tan, M. Askerka, F. Che,  
12 M. Liu, A. Seifitokaldani, Y. Pang, S.-C. Lo, A. Ip, Z. Ulissi and E. H. Sargent,  
13 *Nature*, 2020, **581**, 178-183.
- 14 27. H. S. Jeon, S. Kunze, F. Scholten and B. Roldan Cuenya, *Acs Catalysis*, 2018,  
15 **8**, 531-535.
- 16 28. H. Xu, D. Rebollar, H. He, L. Chong, Y. Liu, C. Liu, C.-J. Sun, T. Li, J. V.  
17 Muntean, R. E. Winans, D.-J. Liu and T. Xu, *Nature Energy*, 2020, **5**, 623-632.
- 18 29. S. Nitopi, E. Bertheussen, S. B. Scott, X. Liu, A. K. Engstfeld, S. Horch, B.  
19 Seger, I. E. L. Stephens, K. Chan, C. Hahn, J. K. Norskov, T. F. Jaramillo and  
20 I. Chorkendorff, *Chem Rev*, 2019, **119**, 7610-7672.
- 21 30. S. Popovic, M. Bele and N. Hodnik, *Chemelectrochem*, 2021, **8**, 2634-2639.
- 22 31. S. Garg, M. R. Li, A. Z. Weber, L. Ge, L. Y. Li, V. Rudolph, G. X. Wang and T.  
23 E. Rufford, *Journal of Materials Chemistry A*, 2020, **8**, 1511-1544.
- 24 32. P. Ramadhany, Q. Luong, Z. Zhang, J. Leverett, P. Samori, S. Corrie, E. Lovell,  
25 I. Canbulat and R. Daiyan, *Advanced Materials*, 2024, **36**, 2405029.
- 26 33. D. Gao, R. M. Arán-Ais, H. S. Jeon and B. Roldan Cuenya, *Nature Catalysis*,  
27 2019, **2**, 198-210.
- 28 34. S. You, J. Xiao, S. Liang, W. Xie, T. Zhang, M. Li, Z. Zhong, Q. Wang and H.  
29 He, *Energy & Environmental Science*, 2024, **17**, 5795-5818.
- 30 35. B. Chang, H. Pang, F. Raziq, S. Wang, K.-W. Huang, J. Ye and H. Zhang,  
31 *Energy & Environmental Science*, 2023, **16**, 4714-4758.
- 32 36. J. Gao, A. Bahmanpour, O. Kröcher, S. M. Zakeeruddin, D. Ren and M. Grätzel,  
33 *Nature Chemistry*, 2023, **15**, 705-713.
- 34 37. S. Kumari, S. Pishgar, M. E. Schwarting, W. F. Paxton and J. M. Spurgeon,  
35 *Chemical communications*, 2018, **54**, 13347-13350.
- 36 38. S. Mori and L. L. Tun, *Plasma Processes and Polymers*, 2017, **14**, 1600153.
- 37 39. S. Ringe, E. L. Clark, J. Resasco, A. Walton, B. Seger, A. T. Bell and K. Chan,  
38 *Energy & Environmental Science*, 2019, **12**, 3001-3014.
- 39 40. B. Huang, K. H. Myint, Y. Wang, Y. Zhang, R. R. Rao, J. Sun, S. Muy, Y.  
40 Katayama, J. Corchado Garcia, D. Fraggedakis, J. C. Grossman, M. Z. Bazant,  
41 K. Xu, A. P. Willard and Y. Shao-Horn, *The Journal of Physical Chemistry C*,  
42 2021, **125**, 4397-4411.
- 43 41. M. C. O. Monteiro, F. Dattila, B. Hagedoorn, R. García-Muelas, N. López and  
44 M. T. M. Koper, *Nature Catalysis*, 2021, **4**, 654-662.
- 45 42. G. Marcandalli, M. C. O. Monteiro, A. Goyal and M. T. M. Koper, *Accounts of*  
46 *Chemical Research*, 2022, **55**, 1900-1911.
- 47 43. A. Xu, N. Govindarajan, G. Kastlunger, S. Vijay and K. Chan, *Accounts of*  
48 *Chemical Research*, 2022, **55**, 495-503.
- 49 44. J. C. Bui, C. Kim, A. J. King, O. Romiluyi, A. Kusoglu, A. Z. Weber and A. T.  
50 Bell, *Accounts of Chemical Research*, 2022, **55**, 484-494.



- 1 45. M. R. Singh, Y. Kwon, Y. Lum, J. W. Ager, III and A. T. Bell, *Journal of the*  
2 *American Chemical Society*, 2016, **138**, 13006-13012. View Article Online  
DOI: 10.1039/C5EE01488C
- 3 46. M. Gattrell, N. Gupta and A. Co, *Journal of Electroanalytical Chemistry*, 2006,  
4 **594**, 1-19.
- 5 47. O. Ayemoba and A. Cuesta, *ACS applied materials & interfaces*, 2017, **9**,  
6 27377-27382.
- 7 48. Q. Wu and Z. J. Xu, *Angewandte Chemie International Edition*, 2025, **64**,  
8 e202505022.
- 9 49. J. M. Yoo, J. Ingenmey, M. Salanne and M. R. Lukatskaya, *Journal of the*  
10 *American Chemical Society*, 2024, **146**, 31768-31777.
- 11 50. D. H. Mei and X. Tu, *J Co2 Util*, 2017, **19**, 68-78.
- 12 51. H. Chen, Y. Mu, Y. Shao, S. Chansai, S. Xu, C. E. Stere, H. Xiang, R. Zhang,  
13 Y. Jiao, C. Hardacre and X. Fan, *Catalysis Science & Technology*, 2019, **9**,  
14 4135-4145.
- 15 52. C. Charalambous, S. Xu, S. Ding, S. Chansai, E. Asuquo, A. Torres Lopez, C.  
16 M. A. Parlett, J. D. Gilmour, A. Garforth and C. Hardacre, *Frontiers in Chemical*  
17 *Engineering*, 2022, **4**.
- 18 53. C.-j. Liu, G.-h. Xu and T. Wang, *Fuel Processing Technology*, 1999, **58**, 119-  
19 134.
- 20 54. S. S. Xu, H. H. Chen, C. Hardacre and X. L. Fan, *J Phys D Appl Phys*, 2021,  
21 **54**, 233001.
- 22 55. C. Mas-Peiro, H. Quinteros-Lama, J. O. Pou and F. Llovell, *Journal of Chemical*  
23 *& Engineering Data*, 2023, **68**, 1376-1387.
- 24 56. S. Xu, H. Chen, C. Hardacre and X. Fan, *Journal of Physics D: Applied Physics*,  
25 2021, **54**, 233001.
- 26 57. A. Mukhtar, S. Saqib, D. Mohotti, R. Ndeddy Aka, Jr., M. Hossain, E. Agyekum-  
27 Oduro and S. Wu, *Environmental Science and Pollution Research*, 2025, **32**,  
28 27314-27334.
- 29 58. D. Wakerley, S. Lamaison, J. Wicks, A. Clemens, J. Feaster, D. Corral, S. A.  
30 Jaffer, A. Sarkar, M. Fontecave, E. B. Duoss, S. Baker, E. H. Sargent, T. F.  
31 Jaramillo and C. Hahn, *Nature Energy*, 2022, **7**, 130-143.
- 32 59. R. Snoeckx and A. Bogaerts, *Chemical Society Reviews*, 2017, **46**, 5805-5863.
- 33 60. A. Bogaerts, A. Berthelot, S. Heijkers, S. Kolev, R. Snoeckx, S. Sun, G.  
34 Trenchev, K. Van Laer and W. Wang, *Plasma Sources Science and*  
35 *Technology*, 2017, **26**, 063001.
- 36 61. G. Centi, S. Perathoner and G. Papanikolaou, *J Co2 Util*, 2021, **54**, 101775.
- 37 62. R. E. Vos, J. P. Smaak and M. T. M. Koper, *Journal of Catalysis*, 2024, **436**,  
38 115613.
- 39 63. A. George, B. Shen, M. Craven, Y. Wang, D. Kang, C. Wu and X. Tu,  
40 *Renewable and Sustainable Energy Reviews*, 2021, **135**, 109702.
- 41 64. M.-Y. Song, H. Cho, G. P. Karwasz, V. Kokoouline and J. Tennyson, *Journal of*  
42 *Physical and Chemical Reference Data*, 2024, **53**, 033102.
- 43 65. K. R. Rasmi, S. C. Vanithakumari, R. P. George and U. Kamachi Mudali,  
44 *Journal of Materials Engineering and Performance*, 2014, **23**, 1673-1679.
- 45 66. T. Yan, X. Chen, L. Kumari, J. Lin, M. Li, Q. Fan, H. Chi, T. J. Meyer, S. Zhang  
46 and X. Ma, *Chemical Reviews*, 2023, **123**, 10530-10583.
- 47 67. J. Hu and F. Liu, *Advanced Energy and Sustainability Research*, 2025, **6**,  
48 2400339.
- 49 68. F. Wang, B. Wang, T. Zhang and J. Liu, *Green Carbon*, 2025.



- 1 69. M. Dauda, J. Hendershot, M. Bello, J. Park, A. Loaiza Orduz, N. Lombardo, O. Kizilkaya, P. Sprunger, A. Engler, C. Plaisance and J. Flake, *Journal of the Electrochemical Society*, 2024, **171**. View Article Online  
DOI: 10.1039/D3SE01488C
- 2
- 3
- 4 70. J.-Y. Kim, K. Anderson, A. Park, J. Simon and L. R. Winter, *ECS Meeting Abstracts*, 2024, **MA2024-01**, 1420.
- 5
- 6 71. C. De Bie, J. van Dijk and A. Bogaerts, *The Journal of Physical Chemistry C*, 2016, **120**, 25210-25224.
- 7
- 8 72. C. C. Jen, J. H. Hsieh and W. Wu, *IEEE Transactions on Plasma Science*, 2024, **52**, 2948-2958.
- 9
- 10 73. N. S. Romero Cuellar, K. Wiesner-Fleischer, M. Fleischer, A. Rucki and O. Hinrichsen, *Electrochimica Acta*, 2019, **307**, 164-175.
- 11
- 12 74. B. Ruqia, G. M. Tomboc, T. Kwon, J. Kundu, J. Y. Kim, K. Lee and S.-I. Choi, *Chem Catalysis*, 2022, **2**, 1961-1988.
- 13
- 14 75. M. Choi, S. Bae, Y. Kim, Y. Lee, M. Cho, S. Kang and J. Lee, *Nature Catalysis*, 2025, **8**, 476-486.
- 15
- 16 76. G. O. Larrazábal, A. J. Martín and J. Pérez-Ramírez, *The Journal of Physical Chemistry Letters*, 2017, **8**, 3933-3944.
- 17
- 18 77. T. Nozaki, X. Chen, D.-Y. Kim and C. Zhan, *Plasma Chemistry and Plasma Processing*, 2023, **43**, 1385-1410.
- 19
- 20 78. L. Liu, J. Dai, Z. Yang, Y. Li, X. Su and Z. Zhang, *Chemical Engineering Journal*, 2022, **431**.
- 21
- 22 79. J. Wan, H. Zhang, J. Zheng, B. Lan, Y. Gang, Q. Huang and X. Li, *Carbon Capture Science & Technology*, 2024, **11**, 100197.
- 23
- 24 80. Y. Yao, T. Shi, W. Chen, J. Wu, Y. Fan, Y. Liu, L. Cao and Z. Chen, *Nature Communications*, 2024, **15**, 1257.
- 25
- 26



The data supporting this article are available at Science DB (<http://www.scidb.cn>), DOI: 10.57760/sciencedb.31168, CSTR: 31253.11.sciencedb.31168.

View Article Online  
DOI: 10.1039/D5SE01488C

Open Access Article. Published on 10 April 2026. Downloaded on 4/10/2026 10:52:24 PM.  
This article is licensed under a Creative Commons Attribution 3.0 Unported Licence.

